Spectral induced polarization of limestones: time domain field data, frequency domain laboratory data and physicochemical rock properties

Johansson, Sara; Lindskog, Anders; Fiandaca, Gianluca; Dahlin, Torleif

Published in:
Geophysical Journal International

DOI:
10.1093/gji/ggz504

2020

Document Version:
Publisher's PDF, also known as Version of record

Geophysical Journal International

Geophys. J. Int. (2020) **220,** 928–950
Advance Access publication 2019 November 05
GJI Marine geosciences and applied geophysics

doi: 10.1093/gji/ggz504

Spectral induced polarization of limestones: time domain field data, frequency domain laboratory data and physicochemical rock properties

Sara Johansson,[1] Anders Lindskog,[2] Gianluca Fiandaca [3] and Torleif Dahlin[1]

[1]*Division of Engineering Geology, Lund University, P.O. Box* 118, *SE*-21100 *Lund, Sweden. E-mail: sara.johansson@tg.lth.se*
[2]*Department of Geology, Lund University, Sölvegatan* 12, *SE*-22362 *Lund, Sweden*
[3]*Department of Geoscience, Aarhus University, C.F. Möllers Allé* 4, *DK*-8000, *Aarhus C, Denmark*

Accepted 2019 November 2. Received 2019 November 1; in original form 2019 February 8

SUMMARY

With advances in data acquisition and processing methods, spectral inversion of time domain (TD) induced polarization (IP) data is becoming more common. Geological interpretation of inverted spectral parameters, for instance Cole–Cole parameters, often relies on results from systematic laboratory measurements. These are most often carried out with frequency domain (FD) systems on sandstone samples. However, the two different methods of measuring the spectral IP response differ in both measurement technique and scale. One of the main objectives of this study is, thus, to perform a direct comparison of inverted spectral parameters from TD IP field data with FD IP spectra from laboratory measurements. To achieve this, field measurements were carried out before a ∼50-m-long rock core was drilled down along one of the measurement lines. Solid parts of the core were vacuum-sealed in plastic bags to preserve the natural groundwater in the samples, after which the core samples were measured with FD spectral IP in laboratory. The results showed that the inverted Cole–Cole parameters closest to the borehole were comparable to the IP spectra measured at the core samples, despite differences in measurement techniques and scale. The field site chosen for the investigation was a limestone succession spanning over a well-known lithological boundary (the Cretaceous–Palaeogene boundary). Little is known in previous research about varying spectral IP responses in limestones, and an additional objective of this study was, therefore, to investigate possible sources of these variations in the laboratory. The IP spectra were interpreted in light of measured lithological and physicochemical properties. The carbonate texture differed strongly across the Cretaceous–Palaeogene boundary from fine-grained calcareous mudstone (Cretaceous) to more well-lithified and coarse-grained wackestone and packstone (Palaeogene). Both laboratory and field spectral IP results showed that these differences cause a large shift in measured bulk conductivity across the boundary. Furthermore, carbonate mound structures with limestone grains consisting mainly of cylindrical bryozoan fragments could be identified in the inverted Cole–Cole parameters as anomalies with high relaxation times. A general conclusion of this work is that limestones can give rise to a wide range of spectral responses. The carbonate texture and the dominant shape of the fossil grains seem to have important control over the electrical properties of the material. A main conclusion is that the inverted Cole–Cole parameters from the field scale TD IP tomography were comparable to the magnitude and shape of FD IP spectra at low frequencies. This opens up large interpretational possibilities, as the comprehensive knowledge about relationships between lithological properties and IP spectra from laboratory research can be used for field data interpretation.

Key words: Electrical properties; Microstructure; Core; Tomography.

INTRODUCTION

Direct current resistivity and induced polarization (IP) are efficient geophysical methods for large-scale characterization of electrical properties in the ground. Recent developments of time domain (TD) instrumentation, data acquisition and processing methods have led to improved possibilities to invert TD IP data for spectral IP (SIP) parameters. Therefore, spectral inversion is becoming more common for various applications, for example detection of contaminated ground (Maurya *et al.* 2018a), bedrock characterization (Johansson *et al.* 2016) and permafrost monitoring (Doetsch *et al*. 2015).

TD IP data are conventionally quantified by the chargeability parameter, which is a measure of the magnitude of the IP. The idea behind spectral inversion is to extract additional parameters describing also the shape of the TD IP decay curves, for example Cole–Cole parameters (Pelton *et al.* 1978). These spectral parameters are expected to be sensitive to textural properties in the ground that are not detectable with resistivity or chargeability alone. It is known, for example, that one of the spectral IP parameters, the relaxation time, is related to the distribution of grain and/or pore throat sizes in the geological material (e.g. Titov *et al.* 2002; Revil *et al.* 2012). These type of links between material properties and IP spectra have been found through controlled laboratory measurements of granular materials, most often carried out with frequency domain (FD) systems (e.g. Scott & Barker 2003; Binley *et al.* 2005; Zisser *et al.* 2010a; Weller *et al.* 2015).

While FD systems are well tested and evidently robust for laboratory measurements, TD systems are in other aspects advantageous over FD systems for large-scale field measurements. Most significantly, TD measurements are several times faster to perform, and measured signal levels can be improved, for example by the use of nested arrays and powerful current transmissions (Dahlin 2014; Zarif *et al.* 2017; Fiandaca 2018). Although spectral TD and FD measurements are theoretically equivalent via the Fourier transform (e.g. Shuey & Johnson 1973), few studies have provided experimental evidence of this equivalence in the context of SIP measurements. An early attempt was made by Zonge *et al.* (1972), who compared traditional TD IP and FD IP parameters measured on samples. During the 1980s and 1990s, Johnson (1984) and Vanhala (1992) compared and found similarities between apparent Cole–Cole parameters measured with FD and TD systems at the same field sites. More recently, a field comparison of inverted Cole–Cole parameters from TD IP and FD IP data acquired along the same profile was presented by Maurya *et al.* (2018b).

To the best of our knowledge, there are yet no studies focusing on a comparison between SIP data from TD field measurements and FD laboratory measurements. Such a comparison is highly relevant as the interpretation of spectral parameters from TD field data to a large degree depends on knowledge gained from laboratory FD SIP research. However, an interpretational extrapolation from relationships established for laboratory FD IP spectra to field TD IP data inverted for spectral parameters is not straightforward and needs to be justified, for two main reasons: (1) The measurements are made in different physical domains (time versus frequency). In practice, factors such as the type of transmitted current waveform and noise might affect the accessible spectral range of TD and FD systems differently. While the spectral range is directly related to the frequency range in FD systems, the accessible spectral range of IP data from TD systems is mainly dependent on the square wave pulse length, the sampling frequency and the rate of the current switch. (2) The measurements are performed on two completely different scales. While relatively homogeneous samples can be used for laboratory measurements, each data point in field data commonly represents a unit volume of several metres. The properties of this unit volume are more or less heterogeneous, which means that spectral responses with different origin can overlap in both apparent and inverted IP decays.

One of the main objectives of the current study is, thus, to perform a direct comparison of inverted SIP parameters from TD IP field data with FD IP spectra from laboratory measurements. The aim is to gain insights into similarities and differences between the two types of SIP measurements. The expected outcome of this contribution is that it can help bridge the current gaps in the research field between field and laboratory measurements as well as between TD SIP and FD SIP measurements.

To achieve a direct comparison of this kind, field TD IP data were first collected and thereafter a (vertical) core drilling was performed along one of the TD IP measurement profiles. Solid parts of the drill core were used for FD SIP measurements in the laboratory, and the physicochemical characteristics of the analysed rocks were examined with a variety of qualitative and quantitative techniques. A field site with a limestone succession spanning a marked lithologic boundary (located approximately 25 m below the ground surface) was chosen for the investigation. Limestone is, in contrast to, for example, crystalline bedrock, an appropriate geological material for our purposes as laboratory SIP measurements require that a measureable amount of current can be transmitted through solid cores. Therefore, the typically low porosity and high resistivity of fresh crystalline rocks complicates the possibilities of obtaining high quality SIP data in laboratory for measurement technical reasons. An additional reason for selecting a limestone site is that little is known about spectral IP responses of limestones in comparison to the comprehensive experience in the SIP community from siliciclastic sedimentary rocks such as sandstones. The relatively large number of previous laboratory FD IP studies on sandstones has resulted in a general understanding of why variations in spectral IP parameters are observed in this type of material. For limestone, however, more research is needed to understand and interpret the variations in SIP parameters that can be observed in field investigations (e.g. Johansson *et al.* 2016). Few publications concerning systematic SIP laboratory studies of different types of carbonate samples (Halish *et al.* 2014; Hupfer *et al.* 2017; Norbisrath *et al.* 2018) or calcite precipitation in sample columns (Wu *et al.* 2010; Zhang *et al.* 2012) exist to date.

Therefore, an additional objective of this study is to investigate if and how well inverted SIP parameters can be used to generalize lithological properties of carbonate rocks at the field scale. The first step is an analysis of variations in laboratory FD IP spectra in light of qualitative and quantitative physical and chemical rock properties, in order to investigate the lithological origin of varying spectral responses in limestone. The second step involves an analysis and evaluation of possible differences between interpretation of laboratory FD SIP and field TD IP data inverted for spectral parameters. The aim and expected outcome is to aid the interpretation of inverted SIP parameters from future field surveys in carbonate environments. Overall, the results are also expected to contribute to the general understanding of SIP responses in geological materials.

GEOLOGICAL SETTING

The limestone succession investigated in this study is situated in the Limhamn quarry, an abandoned open-pit mine in Malmö, southernmost Sweden (Fig. 1). Limestone was mined there for the ce-

Figure 1. Satellite image of the investigated area located at the second floor of the Limhamn quarry, southern Sweden. The locations of the TD IP profiles are shown with black markers, which represent the positions of the electrodes. The red circle marks the position of the drill core.

ment industry until the mid 1990s and today the quarry area is designated as a nature reserve, with lime steppe vegetation, wetlands and animal habitats (Länsstyrelsen i Skåne län 2016). The quarry spans an area of approximately 1.3 km × 0.7 km and reaches approximately 60 m down from the local ground level. The level of the natural ground surface is located at approximately 4 metres above mean sea level (mamsl) at the western edge of the quarry and 12 mamsl at the eastern edge. The northern and southern elevations are approximately 9–10 mamsl and 7–8 mamsl, respectively. The mining operations left three distinct levels in the quarry, at approximately −15 to −20 mamsl, −35 to −40 mamsl and −50 to −60 mamsl (previously, the central quarry floor reached even deeper, but it has been filled with debris; see below). The investigated area is located in the southeastern part of the quarry, at the second 'floor' where the elevation is approximately −40 mamsl.

The boundary between the Cretaceous (Maastrichtian Stage) and the Palaeogene (Danian Stage) geologic time periods, most famous for its coincidence with the extinction of non-avian dinosaurs (e.g. Brusatte *et al.* 2015, and references therein), is found at about −60 mamsl in the Limhamn quarry. Prior to the termination of the mining activities, this boundary was visible above the deepest quarry floor (e.g. Brotzen 1959; Bergström *et al.* 1982, and references therein), but today it is covered by infilled debris. This deepest level part of the quarry hosts wetlands today. Below the Cretaceous–Palaeogene (K–Pg) boundary, the Maastrichtian chalk of the Höllviken Formation (Kruseberg Member) is generally very fine-grained with few macrofossils. Greyish clayey layers, typically 0.1–0.3 m thick, occur (Brotzen 1959; Sivhed *et al.* 1999).

The K–Pg boundary marks an abrupt change in lithology. Above the boundary and upwards towards the natural ground surface, the rock consists of the Danian limestone of the Höllviken Formation (Limhamn member; see below). During the time of deposition, southwestern Scania and large parts of Denmark were covered by a sea. The oldest parts of the Danian limestone consists of bioherm structures, that is ridges or mounds of biologically produced limestone formed at the ancient sea floor (Brotzen 1959; Thomsen 1976). The Danian limestone is generally dominated by fine-grained material, but with more abundant macrofossils (commonly bryozoans) compared to the Cretaceous deposits. The limestone is very hard close to the K–Pg boundary, but less well lithified (i.e. softer) upsection. Flint beds and nodules occur throughout the local limestone succession, but are especially prominent at some stratigraphic levels of the Danian (e.g. Brotzen 1959).

The lithology varies distinctly within the Danian limestone and this interval is thus subdivided into the Limhamn Member (locally recognized 'lower and middle Danian') and the superjacent Köpenhamn Member ('upper Danian') (Brotzen 1959; Sivhed *et al.* 1999). In the Limhamn quarry, the lower Danian is around 10 m thick and located at ∼−60 to −50 mamsl while the middle Danian is found at ∼−50 to −10 mamsl. The upper Danian is located ∼−10 mamsl to natural ground level (Brotzen 1959). The lower and middle Danian limestone mainly consists of the aforementioned ridge or mound structures, typically 5–15 m high and 100–200 m long (Sivhed *et al.* 1999). In the lower Danian mounds, the macrofossils are dominated by cylindrical bryozoan fragments in a fine grained matrix (Thomsen 1976). Lenses of coralline limestone and coralline mounds, associated with relatively high biodiversity, occur in the

middle Danian limestone (Brotzen 1959; Bernecker & Weidlich 1990). The middle Danian forms the uppermost part of the succession investigated in this study. The overlying upper Danian is characterized by regularly bedded and fine-grained limestone with fewer bryozoan fragments (Brotzen 1959; Sivhed *et al.* 1999).

METHODS AND MATERIALS

TD IP field data acquisition, processing and inversion

Two crossing TD IP measurement profiles were placed diagonally on the available ground surface in order to maximize the profile lengths and depth penetration (Fig. 1). Four cables with 5 m spaced take outs and a separated cable layout were used in order to reduce capacitive coupling effects (Dahlin & Leroux 2012). The total number of electrodes (made of acid-resistant stainless steel) along each profile was 82, with an inline spacing of 2.5 m, resulting in profile lengths of 202.5 m. Good electrode contact was assured with a Focus 1 test (Ingeman-Nielsen *et al.* 2016). An ABEM Terrameter LS instrument (www.guidelinegeo.com) with a multiple gradient protocol (Dahlin & Zhou 2006) was used for transmitting current and measuring potentials. In total 1603 quadrupoles, with focus depths (i.e. median depths of investigation based on the sensitivity of the quadrupoles) ranging between 1.34 and 33.15 m were measured at each profile. The injected current waveform was a 100 per cent duty cycle (Olsson *et al.* 2015) with 8-s-long pulses. Full-waveform data were collected at a sample rate of 3750 Hz.

The measured TD IP data were preprocessed in order to improve the data by removal of harmonic noise and background drift and extract data from early IP decay times (Olsson *et al.* 2016). The IP decays were gated in 39 logarithmically spaced windows with centre times ranging from 1.13 ms to 7.13 s. The preprocessed data can still contain decays or individual gates affected by non-systematic noise and inductive coupling effects. Furthermore, the current switch commonly affects the earliest gates retrieved from the pre-processing scheme. This effect is easy to identify as a large and sudden increase in potential of the affected gates. Therefore, the preprocessed data were also manually processed in *Aarhus Workbench* (Auken *et al.* 2009).

The data quality of Line 2 was generally very good and did not require any extensive manual data processing, whereas Line 1 contained slightly more noise- or induction-affected decays. The general method for the manual data processing was to remove early time gates with an obvious change of slope as well as late time gates when a change of sign occurred. In a few cases, full IP decays were also removed. These decays were either strongly corrupted by noise or appeared as outliers in the pseudosections. In total 9.5 and 4.0 per cent of the IP decays in Line 1 and Line 2, respectively, were fully removed. In both data sets, the first three gates were removed from all decays (Fig. 2). The first useable time gate was 2.32 ms in both data sets, but the number of gates affected by induction varies strongly with both signal level and geometric factor (Fiandaca 2018). The variation with geometric factor is reflected in Fig. 2; most of the relatively late time gates were removed from decays located at large pseudo depths (i.e. removed time gates between 3.51 and 8.97 ms). The sudden increase in proportion of removed time gates between 8.97 and 11.36 ms can be explained by a jump of several metres in the pseudo depths of the measurement protocol (see pseudosection in Fig. 7).

The processed data were inverted for spectral Cole–Cole model parameters in the *AarhusInv* software (Fiandaca *et al.* 2013, Auken *et al.* 2014). The FD conductivity form of the Cole–Cole model is (Tarasov & Titov 2013):

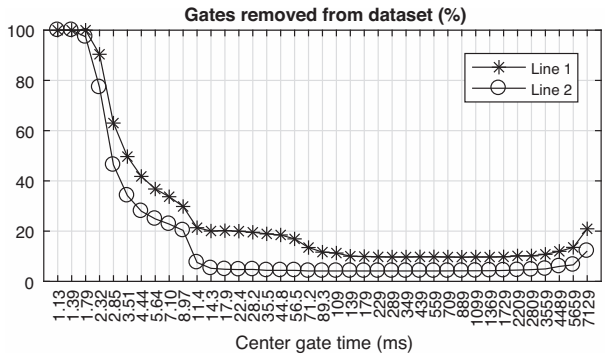

Figure 2. Proportion of centre time gates manually removed from the data sets of Line 1 and Line 2. The number of removed early time gates increase with pseudo depth, but time gates later than 8.97 ms were kept in almost all IP decays. Some of the latest gates can be affected by electrode polarization effects and were therefore removed when they deviated from an otherwise decrementing shape of the decay.

$$\sigma^*(\omega) = \sigma_0 \left[1 + \frac{m_0}{1 - m_0}\left(1 - \frac{1}{1 + (i\omega\tau)^c}\right)\right], \quad (1)$$

where $\sigma^*(\omega)$ is the complex conductivity (S m^{-1}) as a function of angular frequency (rad s^{-1}) and i is the imaginary unit. The Cole–Cole parameters are the low-frequency conductivity, σ_0 (S m^{-1}), the intrinsic chargeability as defined by Seigel (1959), m_0 (mV V^{-1}), the relaxation time, τ(s) and the frequency exponent, c (dimensionless). Fiandaca *et al.* (2018) recently suggested two types of re-parametrizations of the Cole–Cole model in the model space, referred to as the maximum phase angle (MPA) and maximum imaginary conductivity (MIC) parametrizations. In the MIC parametrization, the chargeability m_0 in eq. (1) is exchanged by the maximum imaginary conductivity, σ''_{max} (S m^{-1}). σ''_{max} is defined as the imaginary conductivity value corresponding to the relaxation time τ_σ of the peak in the imaginary conductivity spectrum. This parametrization has two main advantages over the classical Cole–Cole parametrization (eq. 1). Firstly, it is more directly comparable to results of FD SIP measurements and secondly, the depth of investigation (DOI) of the inverted models becomes significantly deeper because of reduced correlations between the different parameters in the model space (Fiandaca *et al.* 2018). The used DOI computation method is described in Fiandaca *et al.* (2015) and takes both data standard deviations and cross-correlations between different model parameters into account.

The used 2-D forward response is a FD complex conductivity response [$\sigma^*(\omega)$] computed from the model parameters (σ_0, σ''_{max}, τ_σ, c) and discretized in a finite element mesh (Fiandaca *et al.* 2013, 2018). The FD forward model is converted to a TD step response for an arbitrary quadrupole via the Hankel transform, and the transmitter waveform is modelled by superposition of step responses (Fiandaca *et al.* 2012). In the iterative inversion process, the L_2 misfit between the data and forward model is minimized for all parameters simultaneously (Fiandaca *et al.* 2013, Auken *et al.* 2014) and the inversion model fit is quantified by a χ misfit value (Fiandaca *et al.* 2018).

The model discretization consists of rectangular blocks divided into columns and rows or layers. We used 23 layers in the inversions with the last depth being 85 m. The number of model columns equals the number of spaces between electrodes and were thus 81

for the data in this study. The vertical and horizontal constraints were set to 2.0 and 1.2, respectively, except for the τ_σ model where a horizontal constraint of 1.6 was used (see Maurya *et al.* 2018b). The noise model in the inversions consist of a standard deviation factor of 1 per cent applied to the resistivity data and a 10 per cent standard deviation factor as well as an absolute voltage noise factor of 0.02 mV V^{-1} applied to the time gates.

Core drilling, borehole logging and groundwater sampling

After a preliminary inspection of inverted TD IP results, the location for the core drilling was determined. The drilling point was placed at the centre of Line 2, see Fig. 1, where relatively strong material contrasts were indicated by the data. The core drilling was performed with the drill rig Riksriggen (Atlas Copco CT20C, www.riksriggen.se), which is a national scientific resource in Sweden financed by the Swedish Research Council and operated by Lund University. Approximately a week after the TD IP measurements, the 6.1-cm-diameter core (Limhamn-2018, stored at the Department of Geology, Lund University) was drilled continuously down to ∼50 m below the local ground surface (i.e. ∼−40 to −90 mamsl). The core was recovered in 3 m long pieces and, apart from some intervals associated with high concentration of flint, the core recovery was nearly 100 per cent. Optical inspection and construction of a preliminary lithological log was continuously carried out in field shortly after the recovery of the core pieces. The limestone varied from competent and solid ∼3-m-long pieces to loose or fragile segments that were broken up before or during the drilling process. All solid portions were vacuum-sealed in plastic bags immediately after the optical inspection, to preserve the natural groundwater in the limestone for the laboratory FD IP measurements.

After the core drilling, the borehole was left to recover for about 1 week. The groundwater level was then determined to 1.8 m below the ground surface. At this stage, the borehole was investigated with different logging methods. A three-arm caliper probe (Robertson Geologging Limited) was used to investigate the borehole diameter and natural gamma radiation along the full borehole depth. Unfortunately, a piece of rock came loose during the caliper probing and blocked the hole. The succeeding logging methods could therefore only reach down to approximately 26 m depth. A temperature-conductivity probe (Robertson Geologging Limited) was used to measure the groundwater conductivity along the borehole, followed by a HIRAT acoustic televiewer probe (Robertson Geologging Limited) and an optical televiewer probe (Robertson Geologging Limited). The acoustic televiewer gives two continuous and detailed ultrasound images of the borehole wall, representing the amplitude and traveltime of the reflected focused ultrasound beam (1.5 MHz piezo-composite transducer). The optical televiewer logging produces a continuous photograph of the borehole wall. The sharp images showed that at the time of the borehole logging, fine materials in the groundwater had settled out of the water column.

A hydrogeological investigation of the site was outside the scope of the study. However, two groundwater samples were collected from the borehole in order to obtain a general picture of the chemical composition. More than 100 l of groundwater were extracted from the borehole with a pump located approximately 25 m below the ground surface. The pump was then lifted to ∼20 and ∼18 m depth where the groundwater was sampled. The samples were sent to an accredited laboratory for analysis of physical and chemical parameters.

FD IP laboratory measurements

In the laboratory, the vacuum-sealed core pieces were unpacked one at a time. The edges of the pieces were cut so that cylindrical samples with flat ends were obtained. Plate current electrodes of stainless steel were placed at both ends of the cylindrical sample. A clamp was used to fix the electrodes to the sample by high mechanical pressure. To further decrease the electrode contact resistances, water soaked porous textile was used between the current electrodes and the sample. The core sample rested on mobile half ring electrodes of stainless steel that were used as potential electrodes. To reduce contact resistances and decrease the risk of electrode polarization errors, water soaked porous textile was also used between the potential electrodes and the sample. Ideally, the potential electrodes should be placed at least twice the sample diameter length from the current electrodes in order to avoid measurement errors caused by electrode polarization at the current electrodes (Zimmermann *et al.* 2008). Furthermore, the potential electrodes are commonly placed at locations 1/3 and 2/3 of the total sample length to ensure that no common mode errors are measured (Zimmermann *et al.* 2008). With a core diameter of 6.1 cm, the ideal sample length is therefore 36.6 cm or more. In this study, the lengths of the samples prepared from the recovered core pieces varied between 17.5 and 46.5 cm (see Table 1). The locations of the potential electrodes were therefore adjusted for each sample in order to reduce the risk of measurement errors as much as possible.

FD IP spectra were measured on each core immediately after they were unsealed from the plastic bags to avoid significant evaporation. The measurement protocol took 52 min to complete and consisted of 64 logarithmically distributed current frequencies between 0.01 and 20 000 Hz. An Ontash PSIP instrument (Version 1.3.1i-2, www.ontash.com) was used for the measurements. A sinusoidal signal with 5 V maximum amplitude was applied on the current electrodes and a 1 kΩ reference resistor. The instrument measures the impedance of the sample, and the complex resistivity is obtained by multiplication of the impedance magnitude with the geometric factor. The obtained parameters are the amplitude- and phase shifts of the received potential sinusoid:

$$\rho^* = |\rho|\ e^{i\varphi}, \tag{2}$$

where ρ^* is the complex resistivity, $|\rho|$ (Ωm) is the resistivity amplitude and φ (rad) is the phase angle. Since resistivity is the reciprocal of conductivity, the measured data can equivalently be expressed as:

$$\sigma^* = |\sigma|\ \ e^{i\varphi} = \sigma' + i\sigma'', \tag{3}$$

where σ^* is the complex conductivity, $|\sigma|$ (S m^{-1}) is the conductivity amplitude and φ (rad) is the phase angle. Expressed in Cartesian coordinates, σ' (S m^{-1}) and σ'' (S m^{-1}) are the real- and imaginary part of the complex conductivity, respectively. In the following, the term FD SIP refer to the σ' and σ'' parameters in eq. (3).

In order to enable a comparison with the inverted TD IP Cole–Cole parameters, the σ'' spectra from the FD IP measurements were fitted with a double Cole–Cole model when applicable. Double Cole–Cole models were only fitted to four out of seven Palaeogene samples for which the spectral shape indicated a polarization peak at low frequencies (the reason for this is that the Cole–Cole model is not applicable for, for example, spectra with constantly increasing shapes). The second peak from the double Cole–Cole model represents the increase in σ'' often observed at higher frequencies in FD IP data (often starting around 10–100 Hz). This

Table 1. Summary of the core samples measured with FD IP together with associated data.

Core sample	Depth (m)	Gravimetric water content (per cent)	Dry density ($g\,cm^{-3}$)	Optical comments	XRF comments	Carbonate texture
P1	2.9–3.3	2.8	2.45	Relatively homogeneous, almost no discernible flint	High in Si	Wackestone (74.5% matrix, 25.7% grains, where of 0.7% glauconite)
P2	5.2–5.4	4.1	2.36	A few flint nodules (light-coloured)		Wackestone (73.5% matrix, 26.5% grains)
P3	6.1–6.5	6.9	2.12	A few flint nodules (light-coloured)		Wackestone (72.2% matrix, 26.7% grains, 1.2% cement)
P4	9.2–9.5	8.0	2.15	Relatively homogeneous, almost no flint		Packstone (39.8% matrix, 58.3% grains, 1.8% cement)with matrix-filled fossil grains
P5	15.8–16.0	2.7	2.40	Relatively homogeneous, fossil grains of visible size	Presence of Al	Packstone-grainstone (30.5% matrix, 57.5% grains where of 1.3% glauconite, 12.3% cement)
P6	18.8–19.3	0.8	2.47	One large band of flint (dark-coloured) and a few smaller nodules (light- and dark-coloured)		Wackestone (69.0% matix, 30.0% grains, 1.0% cement)
P7	20.3–20.5	6.1	2.12	A few flint nodules (light-coloured)		Wackestone (66.7% matrix, 31.7% grains, 1.7% cement)
C1	31.3–31.6	0.6	2.06	Small grain sizes, a few flint nodules (light-coloured)	Presence of Al	Calcareous mudstone (94.0% matrix, 6.0% grains)
C2	37.1–37.5	2.8	2.17	A few flint nodules (light-coloured)	Presence of Al	Calcareous mudstone (87.5% matrix, 12.5% grains)
C3	39.9–40.2	4.0	1.98	Soft and clayey (laminated)	High in Fe, Al, K and Si	Calcareous mudstone (95.8% matrix, 4.2% grains)
C4	43.8–44.1	18.3	1.66	Soft, strongly bioturbated	Presence of Al, high in Si and K	Calcareous mudstone (99.3% matrix, 0.7% grains)
C5	44.1–44.4	18.8	1.65	Soft, strongly bioturbated	Presence of Al, high in Si and K	Calcareous mudstone (99.3% matrix, 0.7% grains)
C6	49.7–50.0	16.6	1.73	Soft, bioturbation		Calcareous mudstone (96.5% matrix, 3.5% grains)

increase could be caused by different mechanisms (additional electrochemical polarization at short length scales, effect of permittivity, Maxwell–Wagner polarization or inductive coupling effects) or a combination of several of these sources. Double Cole–Cole models have been used to fit FD IP spectra in several previous studies (e.g. Pelton *et al.* 1978; Kemna 2000; Zisser *et al.* 2010b; Johansson *et al.* 2019) but other approaches also exist, for example the use of a constant permittivity value representing the high-frequency increase (Kruschwitz *et al.* 2010) or the Debye decomposition method (Nordsiek & Weller 2008). Different forms of the double Cole–Cole models exist, constructed by either a multiplication or a summation of two Cole–Cole relaxations (Major & Silic 1981). In this study, the double Cole–Cole model was represented by a summation of two Cole–Cole relaxations of the same form as presented in eq. (1):

$$\sigma^*(\omega) = \frac{\sigma_0}{2}\left[1 + \frac{m_{0LF}}{1-m_{0LF}}\left(1 - \frac{1}{1+(i\omega\tau_{LF})^{c_{LF}}}\right)\right] \quad (4)$$

$$+ \left[\frac{\sigma_0}{2}\left[1 + \frac{m_{0HF}}{1-m_{0HF}}\left(1 - \frac{1}{1+(i\omega\tau_{HF})^{c_{HF}}}\right)\right]\right.,$$

where m_{0LF}, τ_{LF}, c_{LF}, m_{0HF}, τ_{HF} and c_{HF} are the Cole–Cole parameters representing the relaxation at lower frequencies (LF) and higher frequencies (HF), respectively. Eq. (4) was used to fit the σ'' spectra in the frequency range 0.01–100 Hz using a fixed σ_0 value attained from the

measured σ' data. The quality of the data fit was estimated by calculation of the root mean square error (RMSE):

$$RMSE = \sqrt{\frac{\sum_{i=1}^{N} (x_{O,i} - x_{M,i})^2}{N}}, \quad (5)$$

where x_O are the observed values (i.e. σ'' values measured at different frequencies), x_M are the model values (i.e. the value of the fitted curve at corresponding frequencies) and and N is the total number of measurement points.

Note that it is only the low frequency relaxation of the double Cole–Cole model fit to the laboratory FD IP spectra that is compared with inverted Cole–Cole parameters from the TD IP data in this study. The reason is that a double Cole–Cole model parametrization for TD IP data results in an extremely ill-posed inversion problem when the data span three to four decades in time, as in our field example (three to four decades are actually necessary for well resolving a single Cole–Cole model (Madsen *et al.* 2017). Therefore, the TD field data is only evaluated with a single Cole–Cole model (eq. 1).

Examination of physical and chemical sample properties

The gravimetric water content and dry density of the core samples were estimated by measurements of the sample dimensions and the weight with and without natural pore water. After this, the dry core samples were cut vertically along the length axis (i.e. perpendicular to the bedding) and polished in order to better reveal lithologic/sedimentary details and variations. The interior structure was documented with digital photography before representative portions (together with numerous other samples for reference) were selected for the production of petrographic thin sections. Powders for bulk chemical analyses (∼5–10 g) were collected from each sample using a diamond-tipped electric drill.

Each thin section was carefully examined optically using a petrographic microscope, in order to assess overall qualitative characteristics. The thin sections were also assessed quantitatively using point counting (see Flügel 2010), which provided numeric data on the relative proportions of matrix, grains, and cement. These proportions relate to the so-called carbonate texture, which is broadly comparable to grain size in siliciclastic rocks: Samples with <10 per cent sand-sized and larger grains relative to sedimentary matrix (i.e. the fine-grained muddy material between grains) are referred to as (carbonate) mudstone; samples with >10 per cent grains are called wackestone if the sediment is matrix supported (i.e. grains are generally not in contact); matrix-containing samples with grain supported texture comprise packstone (typically ∼>40 per cent grains relative to matrix); samples with grain supported texture but no matrix between grains comprise grainstone (e.g. Dunham 1962; Flügel 2010). In essence, in the aforementioned order, carbonate textures in unaltered rocks convey a gradually decreasing proportion of matrix relative to grains, generally relatable to increasing water energy in the depositional environment (e.g. Dunham 1962; Flügel 2010). Grains were further categorized as skeletal (consisting of fossil shell material), siliciclastic (consisting of non-carbonate minerals) and lithic (consisting of discernible rock fragments).

Actual grain size distribution—that is numeric data on the physical size of discrete grains—is a notoriously problematic issue within carbonate sedimentology, as it is commonly dependent on the assemblage of rock-forming organisms (see Flügel 2010). Unlike siliciclastic grains, which can be roughly approximated as spheres and behave thereafter in well-developed sedimentary systems, carbonate grains show a vast number of different and commonly complex shapes that lend themselves poorly to simple determination of grain size distributions based on thin sections. Hence, we use carbonate texture as a (somewhat crude) substitute for dominant or average grain size in this study. Carbonate texture should influence SIP results, as different proportions of grains relative to matrix entail differences in rock crystallinity, dry density, porosity, etc. Furthermore, different proportions of grain sizes and shapes are expected to affect both surface chemical properties and polarization length scales.

Chemical data were collected using a Niton XL3t GOLDD handheld X-ray fluorescence (XRF) analyser mounted in a laboratory setup at the Department of Geology, Lund University. Each homogenized sample was subjected to a 240-s analysis routine, wherein data were collected and integrated for the deduction of bulk chemistry. The NIST 2709a San Joaquin soil reference standard (see Mackey *et al.* 2010) was used for monitoring of analytic accuracy and precision.

RESULTS AND INTERPRETATION

Lithological description of the drill core and groundwater chemistry

A simplified profile of the core is shown in Fig. 3(a). The K–Pg boundary was found at ∼24 m below the ground surface (−64 mamsl). The black markers show the approximate locations of black, dense flint bands observed in the optical log, and the yellow sections represent significantly denser sections in the lithology according to the acoustic log. Note that the interpretations of flint-rich and dense limestone sections only cover the uppermost 26 m due to the blockage of the borehole before the optical and acoustic loggings were performed.

Figs 3(b)–(d) show results from the borehole logging. The natural gamma radiation data, which often indicate presence of siliciclastic clay in the bedrock, are depicted in Fig. 3(b). The variation with depth is modest and generally below 10 cps, with occasional peaks with values reaching 15 cps (∼32–33 m) or more than 20 cps (∼38 m) in the Cretaceous limestone. Figs 3(c) and (d) show the results from the groundwater temperature and conductivity logging. The temperature of the groundwater was 5.4 °C at 2 m depth and gradually increased to 9.3 °C at 26 m depth. The increase in groundwater conductivity is most likely related to the temperature increase. Initially, the conductivity increases steeply from 40 to 50 mS m^{-1} between 2 and 2.6 m, followed by a more gradual increase to 59 mS m^{-1} at 26 m depth. The physical and chemical composition of the groundwater samples collected at ∼18 and ∼20 m depth showed mutually consistent results. The mean conductivity was 87.5 ± 0.8 mS m^{-1} (at 25 °C) and the mean pH was 7.8 ± 0.1 (at 20 °C). The major anions in the groundwater samples consisted of sulphate (SO_4^{2-}, mean value 215 ± 7.1 mg l^{-1}) and chloride (Cl^-, mean value 58.5 ± 0.7 mg l^{-1}). Major cations were calcium (Ca^{2+}, mean value 255 ± 106.1 mg l^{-1}), magnesium (Mg^{2+}, mean value 54.5 ± 0.7 mg l^{-1}) and sodium (Na^+, mean value 31.0 ± 0.0 mg l^{-1}).

The labels in Fig. 3(a) show the approximate stratigraphic levels of the core samples that were investigated with FD SIP. The physical properties of the samples varied from poorly lithified and typically fine textured to well lithified and coarse textured limestone. An overview of data associated with the core samples is reported in Table 1. In Figs 4(a)–(m), photographs of the core samples are shown,

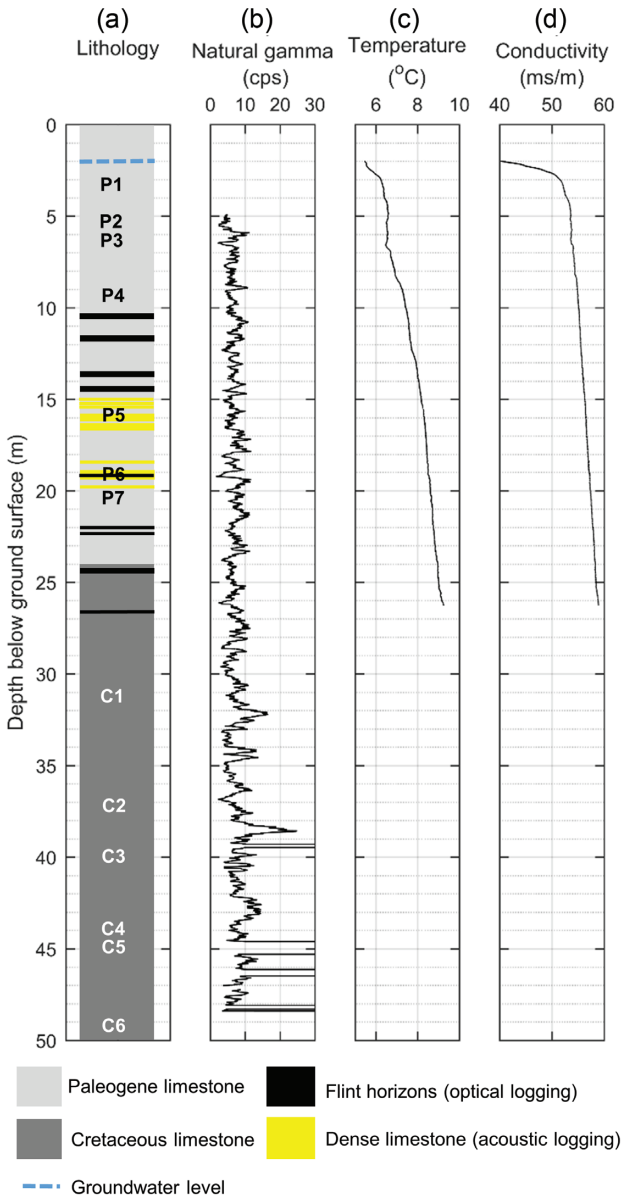

Figure 3. Overview of the lithological variations in the core and borehole logging results. (a) simplified sketch of the main lithological units in the core together with significant features visible in the optical and acoustic logs. The labels show the approximate location of the core samples reported in Table 1. (b) natural gamma variations along the borehole wall. (c) Variations of groundwater temperature and (d) groundwater conductivity.

from which it is evident that the macrostructure of the samples differ. The macrostructures range from, for example, homogeneous material with coarse sand-sized fossil grains (Fig. 4e) to clay-rich laminated structure (Fig. 4j) and matrix-dominated, strongly bioturbated materials (Figs 4k–l). The carbonate texture data obtained from the corresponding thin sections are also reported in Figs 4(a)–(m).

A few general structural differences could be distinguished between the Palaeogene and the Cretaceous samples. The Palaeogene samples were typically better lithified and the carbonate textures were relatively coarse (wackestone and packstone). Although grain size distributions could not be determined from the thin sections, representative sizes of individual grains were measured and were generally below 10 mm. Presence of cement was observed in all Palaeogene thin sections except the two uppermost ones (P1 and P2) and a few samples even retain porosity (mainly P5). In contrast, the Cretaceous samples were less well lithified and had significantly finer carbonate textures (carbonate mudstone). Cement was not observed in any of the Cretaceous thin sections. The XRF results (Table 1) indicate that the matrix-dominated Cretaceous samples in general contained more Al and K compared to the Palaeogene samples, likely reflecting a larger proportion of siliciclastic clay minerals.

Figs 4(n)–(t) show microscopic details in representative thin sections. The carbonate grains in sample P1 (Fig. 4n) consist almost exclusively of bryozoan fragments (with elongated ∼cylindrical shapes), but mollusks, ostracods and foraminifera are also present. The sizes of the bryozoan fragments that appeared to have not been cut diagonally were around 0.3–0.6 mm in diameter and 3–6 mm long. Sample P4 (Fig. 4o) consists of a clearly more diverse fauna. Although bryozoans dominate also at this level, there is also a distinct presence of echinoderms as well as other fragments (e.g. mollusks, ostracods and vertebra). Samples P5 (Fig. 4p) and P6 (Fig. 4q) are reminiscent of P4, but have clearer dominance of bryozoans. As already mentioned, the carbonate textures of the Cretaceous samples (Figs. 4r–t) are distinctly dominated by matrix. Among the few observed carbonate grains, bryozoans dominate in sample C2 (Fig. 4r), while foraminifera, mullusks and ostracods are more common in C6 (Fig. 4t, similar to C4 and C5). Sample C3 (Fig. 4s) clearly deviates from the other Cretaceous samples. In this sample, the grains mainly consist of minute fragments tentatively identified as sponge spicules and the rock is strewn with fine-grained pyrite.

FD SIP results and interpretation

The results of the FD SIP measurements are shown in Fig. 5, with the Palaeogene samples to the left (Figs 5a–c) and the Cretaceous samples to the right (Figs 5d–f). All Palaeogene samples have σ' values ranging between ∼4 and 8 mS m^{-1} except P5 and P6 where the values are very low, below 1 mS m^{-1} (Fig. 5a). Fig. 3a shows that samples P5 and P6 originate from zones with significantly denser limestone. Part of the explanation to the low σ' values in P5 and P6 is probably that the estimated water contents are low while the dry densities are large (Table 1), which together indicate low porosity.

The highest σ' values of the Palaeogene samples, ∼8 mS m^{-1}, were measured on samples P2 and P4 (Fig. 5a). P4 has the highest estimated water content (8 per cent) of the Palaeogene samples and low dry density, indicating relatively high porosity. However, the estimated water content of P2 is only 4.1 per cent. The σ' variations can therefore not be explained only by the water content. Other contributing factors can be found in the textural properties of the samples. Sample P2 has a wackestone carbonate texture with high proportion of matrix (73.5 per cent) compared to the packstone texture of sample P4 (with 39.8 per cent matrix). This difference could explain why similar σ' values were measured on P2 and P4 despite the large differences in water content. The σ' variations between all the Palaeogene samples are probably related to a combination of water content, dry density and carbonate texture.

The measured φ spectra of the Palaeogene samples are shown in Fig. 5(b). P1 and P6 have shapes with evident peaks around 0.2 and 0.8 Hz, respectively. The spectral shape of P5 also resembles a peak at low frequencies, but with a relaxation at a frequency below the measurement range (<0.01 Hz). For these three samples, the φ values start to increase steeply somewhere above 50 Hz. The

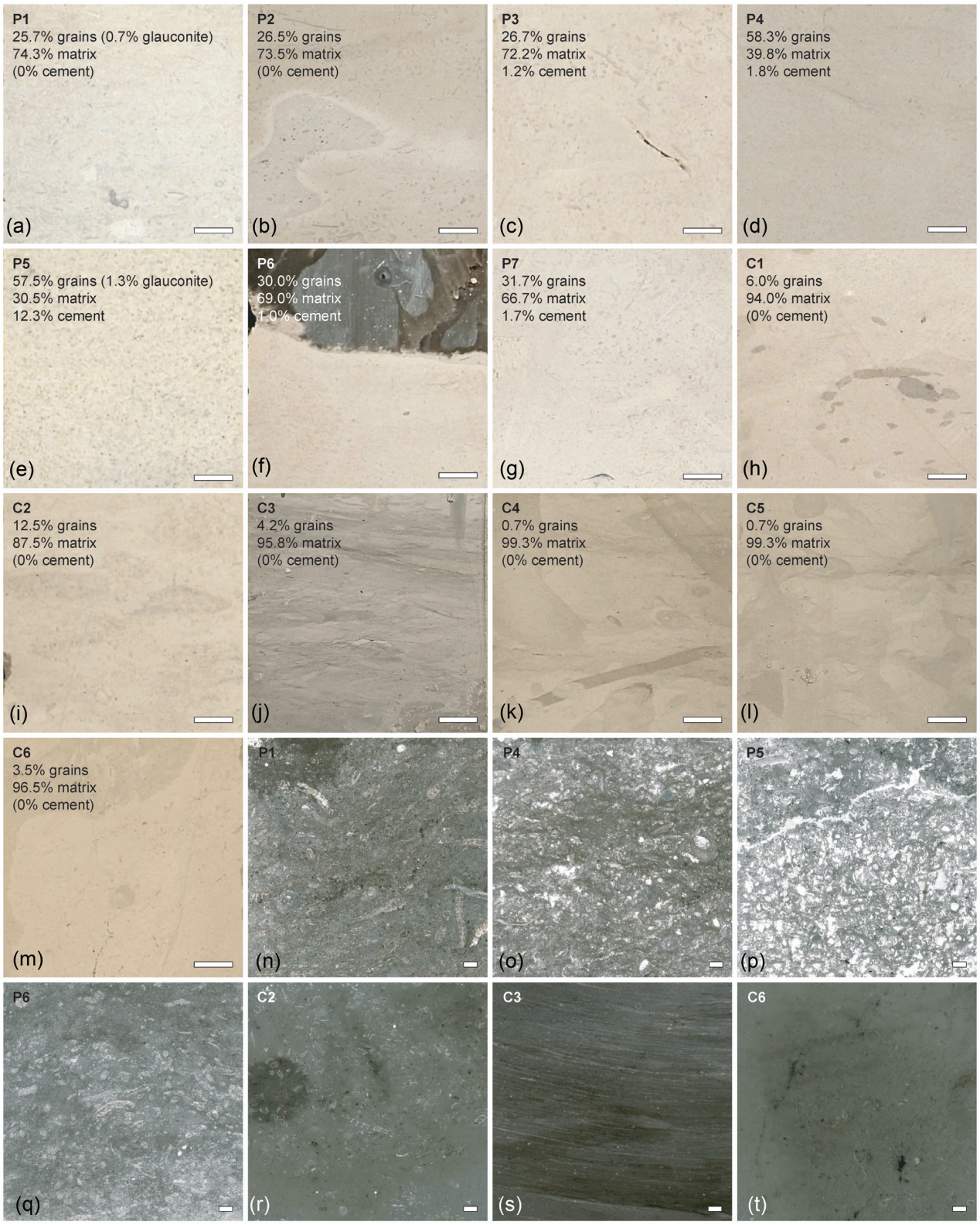

Figure 4. (a–m) Photographs showing the macrostructure of the samples (sample number in upper left of images; see also Table 1) together with data from quantitative thin section examinations (reflected light, scale bar 10 mm). (n–t) A selection of images of representative microscopic facies details (transmitted light, scale bar 1 mm). Sample names are shown in the upper left of the individual images.

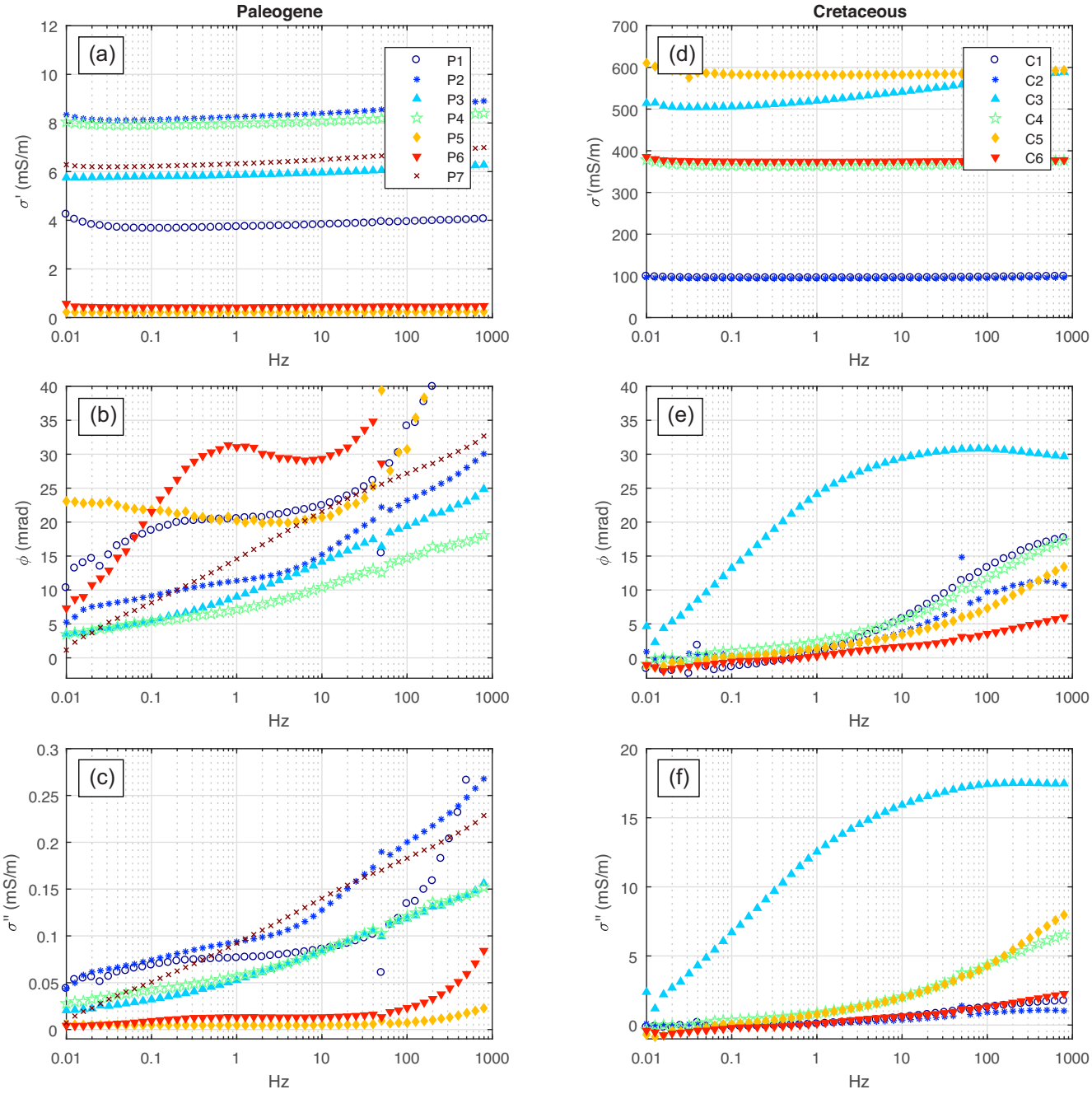

Figure 5. Results of FD IP measurements on the Palaeogene (a–c) and Cretaceous (d–f) samples. Note different scales for σ' (a and d) and σ'' (c and f).

shape of P2 reminds of a possible peak with a broad distribution of relaxation times at low frequencies (<10 Hz). At higher frequencies, however, the increase in φ is more similar to samples P3 and P4. P3 and P4 have spectral responses that gradually increase with frequency. At 0.1 Hz, the φ values are close to −5 mrad for these two samples. In P7, the φ values increase with a constant slope as a function of frequency decade over the entire measurement range. The slope of the increase in φ above 100 Hz is very similar for all the samples P2, P3, P4 and P7, although the magnitude differs.

The strength of the φ response is often proportional to the bulk conductivity in geological materials since higher bulk conductivity generally leads to a less proportion of the current moving through the electrical double layers around the mineral grains (Slater & Lesmes 2002a). It is therefore not surprising that the highest φ values were measured at the samples with the lowest σ' values (P5 and P6). Slater & Lesmes (2002a) showed that σ'' is more sensitive than φ to surface properties at the microscale in the material. Unlike φ, σ'' (which can be approximated by the multiplication of φ with σ') can be assumed to be independent on the bulk conductivity through the pore water in the material (Slater & Lesmes 2002a).

The magnitude and shape of the σ'' spectra, shown in Fig. 5(c), shows a pattern that seems consistent with depositional depth. The spectra of the shallower samples P1 and P2 are characterized by shapes with a peak and relatively high σ'' values at low frequencies (<1 Hz). At deeper levels, samples P3 and P4 have almost identical σ'' spectra that gradually increase with frequency. While the low

frequency σ'' values are intermediate for P3 and P4, they are very low for samples P5 and P6, both of which also indicate a peak at low frequencies. Finally, the deepest sample P7 stands out with a constant increase of σ'' with frequency decade. Some differences and similarities between the physical properties of samples with similar spectra can be found:

- P1 and P2 have carbonate textures with similar proportion of grains (25.7 and 26.5 per cent) and no cement. The dry densities of P1 and P2 are high (2.45 and 2.36 g cm^{-3}) in relation to P3, P4 and P7.
- P3 and P4 have different proportion of grains (26.7 and 58.3 per cent) but similar proportion of cement (1.2 and 1.8 per cent), water content (6.9 and 8.0 per cent) and dry density (2.12 and 2.15 g cm^{-3}).
- P5 and P6 have different proportion of grains (57.5 and 30.0 per cent) but similar physical bulk properties. Both samples have small porosities (2.7 and 0.8 per cent) and high dry densities (2.40 and 2.47 g cm^{-3}). P5 has a large proportion of cement (12.3 per cent) while P6 has large amounts of developed flint.
- P7 is most similar to P3 and P4 in carbonate texture (31.7 per cent grains and 1.7 per cent cement), porosity (6.1 per cent) and dry density (2.19 g cm^{-3}).

In the Cretaceous samples, the σ' values (Fig. 5d) are generally very high (on average 300–400 mS m^{-1}) compared to the Palaeogene samples (note the different scales in the plots). The main reason is probably the fine-grained matrix-dominated texture of all the Cretaceous samples. Only in samples C1 and C2 are the σ' values as low as 100 mS m^{-1}, which is probably caused by the low water contents (0.6–2.8 per cent). Significantly larger water contents—likely bound in/to fine-grained (∼clay sized) minerals—were measured in C4, C5 and C6 (16.6–18.8 per cent). This, in combination with the fine carbonate texture, is probably the reason why the measured σ' values exceeds ∼400 mS m^{-1} in these samples. In sample C3, the measured σ' values are above 500 mS m^{-1} despite the much lower water content (4 per cent). In C3, however, the clayey laminated structure probably contribute to the high σ' values. Twice as high amounts of K and Al was detected with XRF in sample C3, compared to all other samples. This confirms a larger proportion of siliciclastic clay minerals in C3. Furthermore, almost twice the amount of Fe was detected in C3, compared to all other samples, indicating higher presence of conductive minerals (probably mainly pyrite; see above).

The measured φ values (Fig. 5e) are generally much lower for the Cretaceous samples compared to the Palaeogene. Furthermore, the shapes of all the spectra except C3 show a similar pattern with values close to zero below 1 Hz, followed by a gradual increase. The Cretaceous σ'' spectra (Fig. 5f) can be divided into three groups based on magnitude and spectral shape. Although all Cretaceous samples have similar carbonate textures with a domination of matrix grains and absence of cement, some differences and similarities between the groups can be found in the physical bulk properties:

- C1 and C2 have the highest proportion of grains among the Cretaceous samples (6–12.5 per cent) and similar macroscopic structures. Furthermore, the water contents (0.6–2.8 per cent) and densities (2.06–2.17 g cm^{-3}) indicate relatively low porosities in these samples compared to C4, C5 and C6 (>16 per cent and <1.73 g cm^{-3}).
- C3 deviates from all other samples in many aspects; the macroscopic structure is clearly clay-laminated, which is verified by the XRF measurements indicating higher amounts of K and Al compared to all other samples. In addition, the amounts of Fe is almost twice as large as in all other samples.
- C4 and C5 have very similar macroscopic structures with significant bioturbation (Figs 4k–l) and essentially identical carbonate texture. Furthermore, the water content and dry density as well as the bulk chemical composition are almost identical for these two samples. C6 is similar to C4 and C5 in macroscopic structure and carbonate texture. However, the K, Al and Si levels are much lower or absent in C6, indicating significantly lower amounts of siliciclastic clay in C6. The water content and dry density also differ slightly from samples C4 and C5.

Fig. 6 shows σ' and σ'' of all samples at 1 Hz, plotted against gravimetric water content (6a–b), proportion of grains in the carbonate texture (6c–d), Ca content (6e–f), Fe content (6g–h) and K content (6i–j). As already discussed above, the σ' and σ'' values seem to be related to both water content and proportion of grains in the carbonate structure. At 1 Hz, Figs 6(c) and (d) show that the trends in σ' and σ'' looks consistent and strongly related to the carbonate texture. Both σ' and σ'' increase with increasing proportion of fine materials (decreasing grain content) in the sample. Part of the data in Figs 6(e) and (f) indicate a inversely proportional relationship between Ca content and σ'/σ'' values at 1 Hz. Lower Ca content indicates a larger proportion of non-carbonate minerals in the samples (e.g. siliciclastic grains). The negative relationship with both σ' and σ'' values could possibly indicate an effect of the weaker surface charge on calcium carbonate grains compared to other minerals (Zhang *et al.* 2012). While the Fe content and K content show no trends when plotted against the σ' values (Figs 6g and i), weak positively proportional relationships are indicated in Figs 6(h) and (j) when these parameters are plotted against σ''. These trends are not consistent among all samples and depends to a large degree on the Fe and K rich sample C3 as well as the intermediate Fe and K contents in samples C4 and C5. The Fe content indicates conductive minerals in the samples while the K content indicates siliciclastic clay minerals. Thus, the positive trend indicates that σ'' increases with increasing proportion of conductive minerals and clay minerals in the samples.

Results of spectral TD IP tomography and comparison with FD SIP

Figs 7(a)–(c) shows the resistivity and integral chargeability pseudosections as well as the time range of the processed data in Line 2. The integral chargeability (as opposed to the intrinsic chargeability in the Cole–Cole model) is a conventional measure of the mean value of the IP decay, here calculated by taking all of the time gates into account. This measure can conveniently be used for a general assessment of the IP decay data quality distribution in the pseudosections. The smooth distribution of apparent resistivity and chargeability values in Figs 7(a) and (b) indicate good data quality. In Fig. 7(c), the shorter time range of the processed data in the deeper part of the pseudosection is mainly a consequence of larger geometric factors and removal of early time gates described above (compare with Fig. 2). Fig. 7(d) shows the average lateral χ misfit of the resistivity and IP inversion models. The data fit is generally better for the IP data than the resistivity data in the central part of the line. Fig. 7(e) shows the χ misfit corresponding to an early time gate. Early decay times were, as discussed above, only kept in the upper part of the pseudosections, in order to avoid effects of electromagnetic induction. The χ misfit show that the inversion model underestimates the data at early decay times, which is likely an effect of the single Cole–Cole model parameterization used for the inversion. This model does not take into account

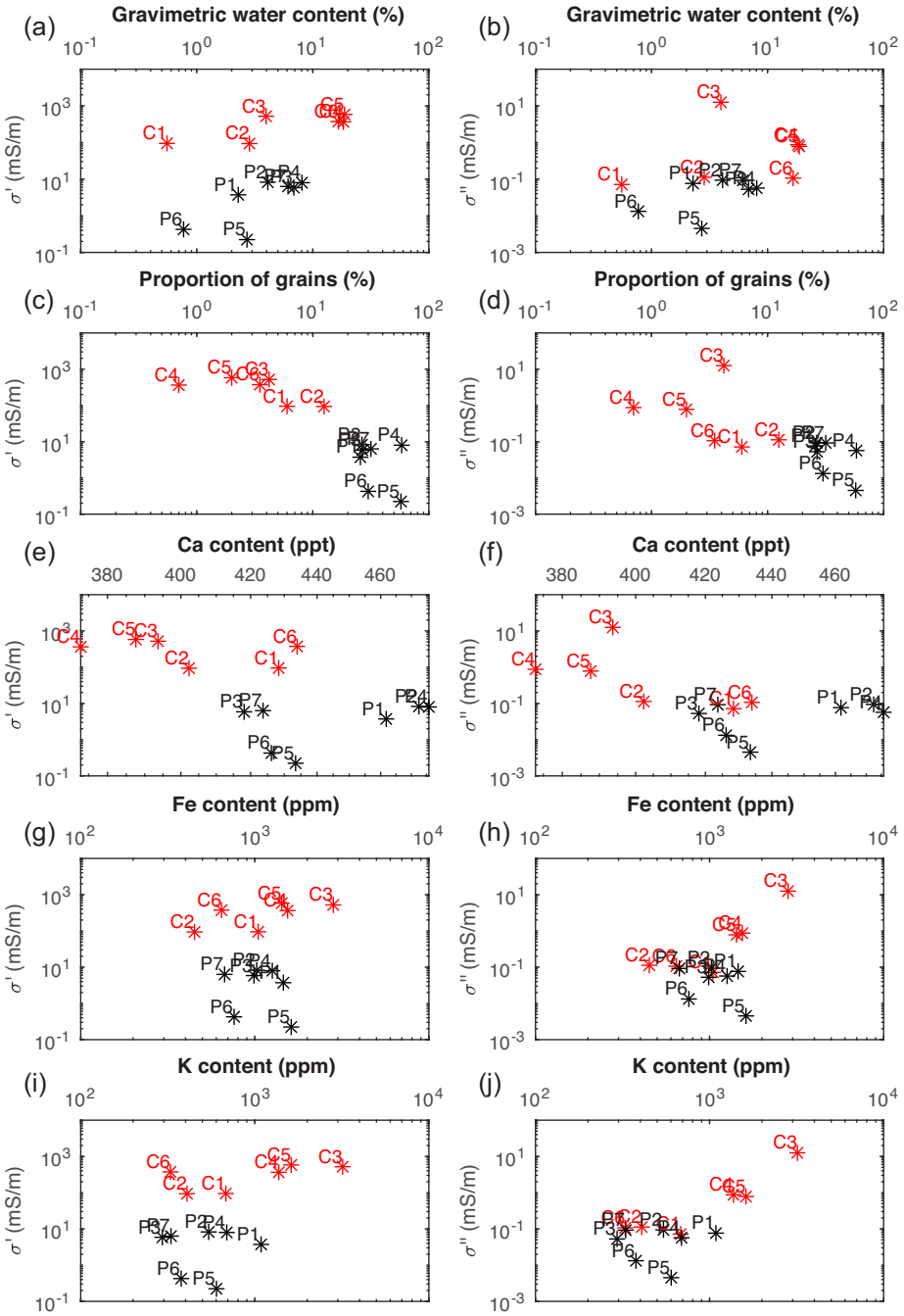

Figure 6. Real conductivity (left-hand panel) and imaginary conductivity (right-hand panel) values at 1 Hz plotted against the gravimetric water content (a, b), proportion of grains in the carbonate texture (c, d) as well as the Ca content (e, f), Fe content (g, h) and K content (i, j) obtained from the XRF measurements. Red and black markers represent Cretaceous and Palaeogene samples, respectively.

spectral shapes with increasing polarization at early times, which can be attributed to dielectric permittivity (Fiandaca 2018) or overlapping high-frequency polarization mechanisms. However, an inversion of the field data in terms of a double Cole–Cole model, necessary for fitting the laboratory data, is not feasible. Indeed, as shown by Madsen *et al.* (2017), an acquisition time range comprised between three to four decades, as in our data, is sufficient for well resolving a single Cole–Cole relaxation. A wider acquisition range, with signal measured at earlier times, would be necessary for interpreting the field data with a double Cole–Cole relaxation.

Fig. 7(f) shows the average χ misfit between the data and the forward model is 1.6 for Line 2 and 1.9 for Line 1 (data from Line 1 are not shown for brevity). In Fig. 7(g), some examples of the fit between data and forward model IP decays are shown. The locations of these IP decays are indicated with coloured square markers in Figs 7(a)–(e).

Fig. 8 shows the inverted conductivity model of Line 2, where a clear magnitude shift can be observed at a depth corresponding to the K–Pg boundary. The dashed horizontal line represents the approximate K–Pg boundary at the location of the borehole. The

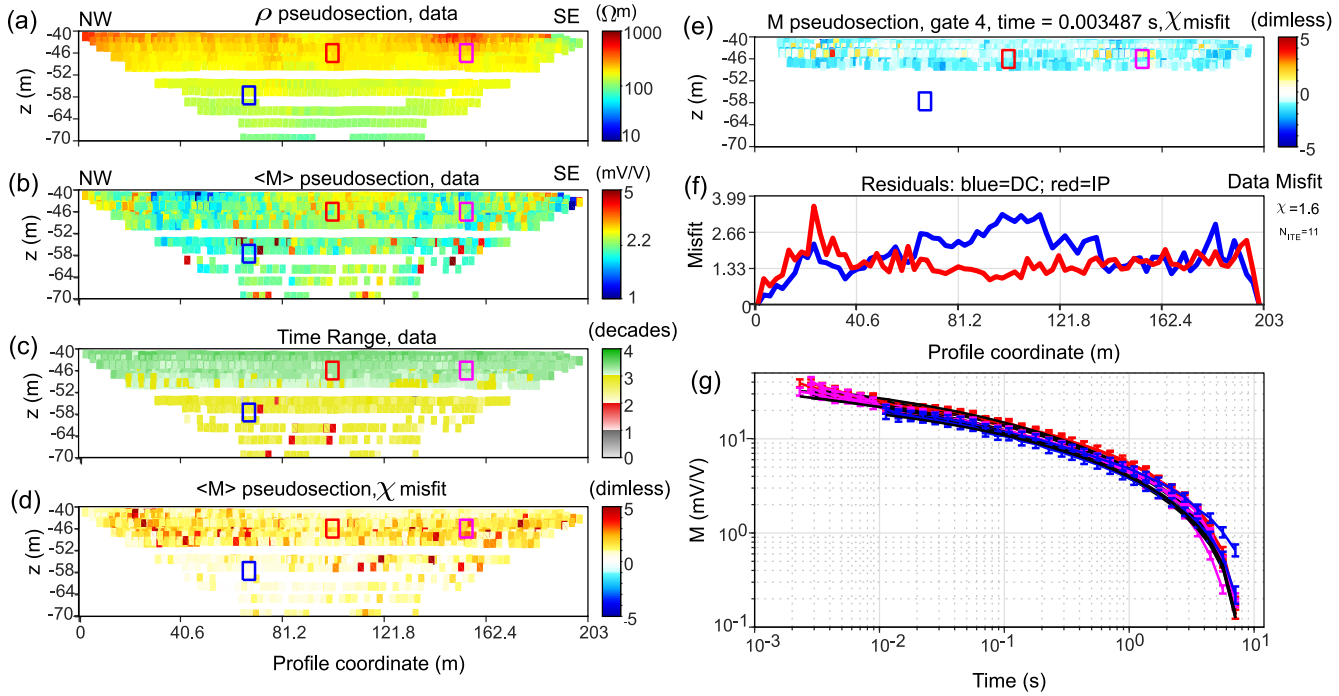

Figure 7. Processed data and inversion model fit of Line 2. (a) Resistivity data pseudosection. (b) Chargeability data pseudosection. (c) Time range of the processed IP data (d) Chi misfit between chargeability data and forward model. (e) Chi misfit between data and forward model at an early time gate showing that the inverted model underestimate the data at early times. (f) Lateral average data misfit. (g) Examples of data and forward model decays.

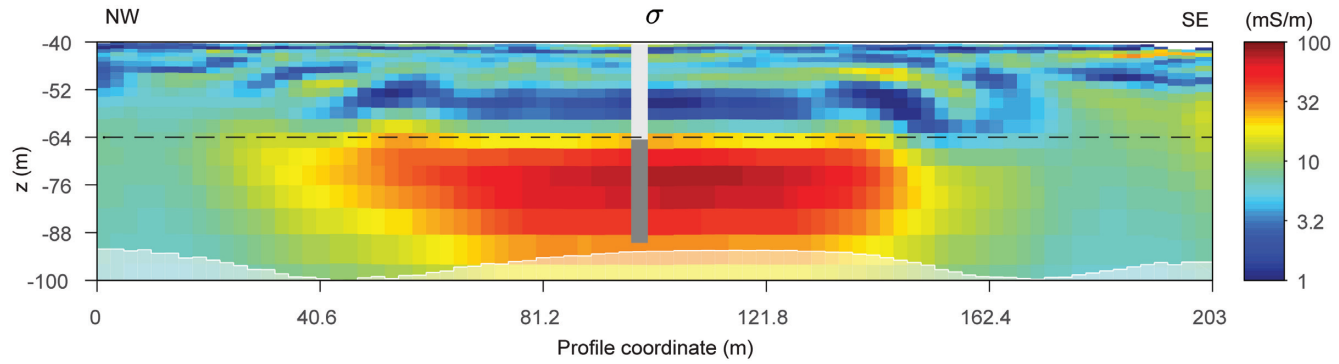

Figure 8. Inverted conductivity model from line 2. The K–Pg boundary is shown at the location of the core and extrapolated with a black dashed line.

conductivity is generally below 10 mS m^{-1} above the boundary, which is in excellent agreement with the σ' data from the laboratory FD SIP measurements on the Palaeogene samples. In the Cretaceous limestone, the inverted conductivity is above 30 mS m^{-1} up to more than 100 mS m^{-1}. These values are below the σ' values measured on the Cretaceous samples, which range between 100 and 600 mS m^{-1}. Nevertheless, the difference between the two general limestone types below and above the boundary is clearly resolved by the field data.

Fig. 9 shows all inverted Cole–Cole parameters of Line 2. The levels below the selected DOI threshold of 5 (see Fiandaca *et al.* 2015) are masked with opaque white colour in Figs 8 and 9. The DOI in the conductivity model is almost 60 m (Fig. 8), while the DOI threshold is located at shallower depths in the Cole–Cole parameters sections (Figs 9b–d). Therefore, only the uppermost 30 m of the inverted models are shown in Fig. 9. Three rectangles (A–C) have been marked on the inverted sections for a comparison with the laboratory FD SIP data. Rectangle A represent the levels of core samples P1 and P2. This area is characterized by σ''_{max} values around 0.07–0.08 mS m^{-1}, τ_σ values around 0.4 s and c values around 0.4 in the inverted models. The inverted σ''_{max} values are in excellent agreement with the σ'' values between 0.01 and 1 Hz from the laboratory FD SIP measurements.

Rectangle B in Figs 9(b)–(d) represent the levels of samples P3 and P4. The σ''_{max} values from the inverted model are around 0.03–0.04 mS m^{-1}, which is in agreement with the σ'' values between 0.01 and 1 Hz from the laboratory FD SIP measurements. The inverted τ_σ and c values are around 0.05 s and 0.45, respectively, while the laboratory data do not indicate Cole–Cole shaped spectra in the samples from these levels.

The levels of samples P5 and P6 are represented by rectangle C in Figs 9(b)–(d). Here, the inverted σ''_{max} values are around 0.02 mS m^{-1}, which is slightly higher than the σ'' values measured on the samples (0.005–0.015 mS m^{-1}). The inverted τ_σ and c values are close to or below the calculated DOI in the inverted models. The inverted values are around 1–5 s for τ_σ and 0.45 for c; the inverted τ_σ

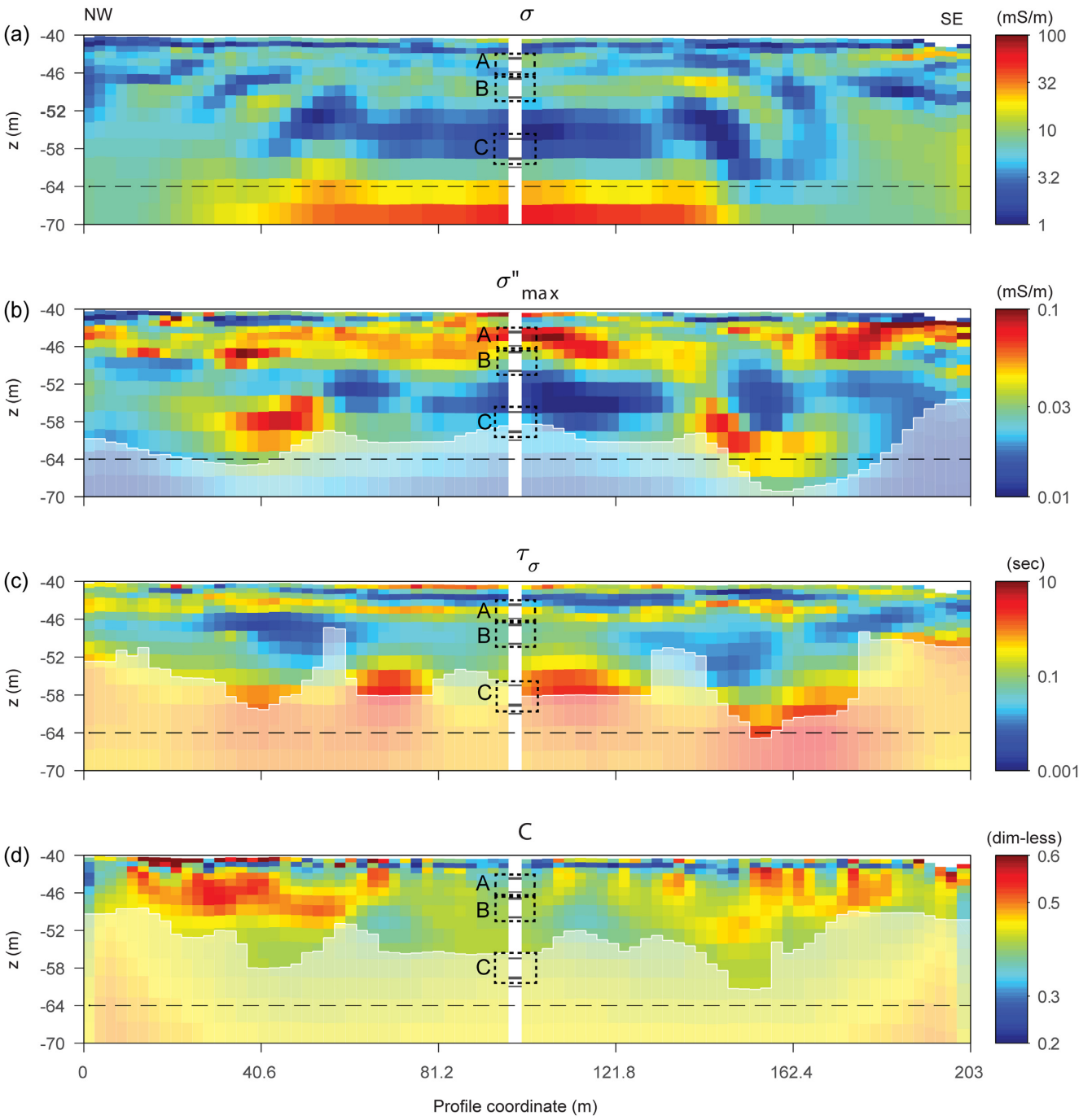

Figure 9. Inverted models from Line 2 with the location of the borehole and the laboratory core samples marked. The horizontal black line represent the K–Pg boundary at the location of the core. (a) Conductivity, (b) imaginary conductivity, (c) relaxation time and (d) frequency exponent.

values are thus in between the values extracted from the laboratory samples from corresponding depths (0.15 and 51 s, respectively, see below).

The levels of sample P7 and all Cretaceous samples are below the DOI of the inverted Cole–Cole sections and are therefore not further discussed in this section. Fig. 10 shows a direct comparison between the FD IP spectra measured on the Palaeogene samples above the DOI (P1–P6) and the inverted TD SIP data from different model cells (layers 4–13). The model cells represent the inverted vertical model closest to the borehole location (model column 40). Fig. 10(a) shows the σ' data measured at the core samples P1 and P2, located in the shallowest Zone A (compare with Fig. 9), together with inverted model cell conductivity values from comparable levels in the bedrock. Figs 10(b) and (c) show corresponding comparisons for Zone B and Zone C, respectively. The σ'' spectra from the laboratory FD IP data are shown in Figs 10(d)–(f), also divided into different subplots representing the bedrock levels in zones A–C. The spectra from samples P1 and P2 (Fig. 10d) as well as P5 and P6 (Fig. 10f) were fitted with double Cole–Cole models and the imaginary parts of the fitted models are shown with turquoise lines. The low frequency (LF) and high frequency (HF) Cole–Cole model from the respective double Cole–Cole model fit have also

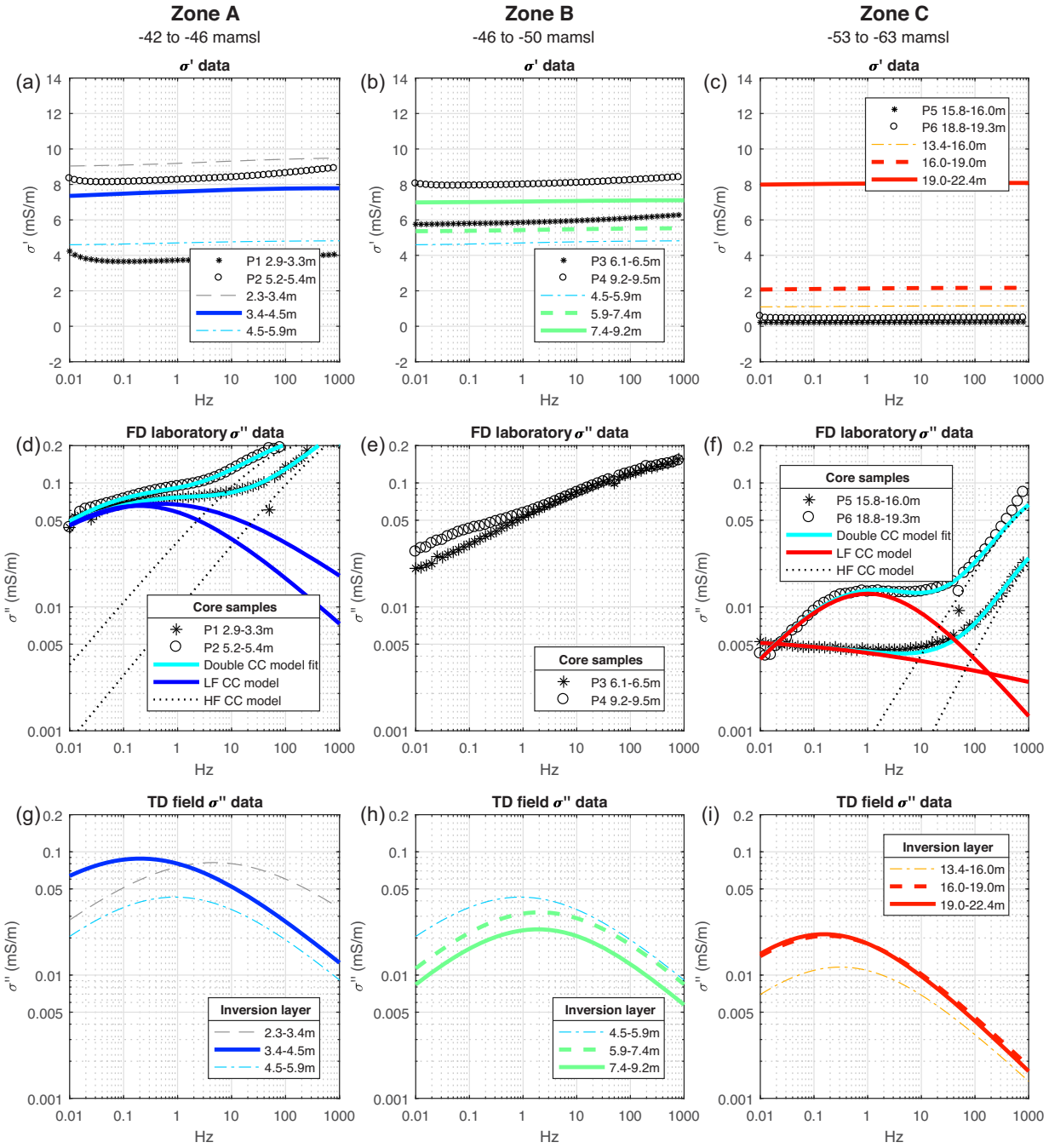

Figure 10. Direct comparison of laboratory FD SIP data and inverted Cole–Cole parameters from field TD IP data. (a–c) Comparisons between the real conductivity spectra at different depths beneath the ground surface (zone A, zone B and zone C, see Fig. 9) and the inverted conductivity values at corresponding depths. (d–f) Imaginary conductivity spectra measured with FD IP in laboratory at different depths beneath the ground surface (zone A, zone B and zone C, see Fig. 9). The spectra in zone A (d) and zone C (f) have been fitted with double Cole–Cole models (turquoise colour). The low- and high frequency relaxations (LF and HF CC models) were then plotted separately in order to enable a comparison between the Cole–Cole-shaped low frequency FD SIP data (blue/red colour) and the inverted Cole–Cole parameters from the TD IP tomography at corresponding depths (g–i). The inverted Cole–Cole parameters in each model cell have been used in eq. (1) to plot the data in FD (g–i).

been plotted in Figs 10(d) and (f) to facilitate a comparison of the LF data with the inverted TD SIP data in Figs 10(g)–(i). The double Cole–Cole parameters extracted from the fitted models are reported together with RMSE values in Table 2. In Figs (g)–(i), the FD Cole–Cole model has been calculated from the inverted Cole–Cole parameters in each model cell using eq. (1).

Due to the relatively coarse discretization of the inverted model cells, it is not always obvious which of the model cells should be compared to the relatively small laboratory samples. This is especially the case if the core samples are located close to the boundary between different model cells with large dimensions. Although the core has been carefully compared with the optical logging results,

Table 2. RMSE values and parameters extracted from the double Cole–Cole model fit of samples P1, P2, P5 and P6.

		Low frequency Cole–Cole model			High frequency Cole–Cole model		
	RMSE (mS m^{-1})	m_0 (dimensionless)	τ (s)	c (dimensionless)	m_0 (dimensionless)	τ (s)	c (dimensionless)
P1	0.0019	0.21	0.28	0.32	0.36	0.00004	0.58
P2	0.0019	0.09	0.83	0.40	0.19	0.0005	0.51
P5	0.00016	0.49	51	0.12	0.37	0.00005	0.77
P6	0.00036	0.18	0.15	0.49	0.40	0.00009	0.74

uncertainty commonly remains in the exact location of the individual core samples as the core recovery was not always 100 per cent. The uncertainty of core sample elevation is estimated to approximately one decimeter. Moreover, the inverted TD SIP data are affected by inversion constraints and a decreasing resolution with increasing depth beneath the ground surface. For these reasons, the inverted model cell layers cover larger depths than the core samples in Figs 10(a)–(c) and (g)–(i).

In Fig. 10(a), the model layer at depth 3.4–4.5 m (bold blue line) represents rectangle A discussed above, which is the model layer in between samples P1 and P2. There is a relatively large increase in measured σ' values between the shallower sample P1 and the deeper sample P2 (Fig. 10a). The σ_0 values of the model cell at 3.4–4.5 m is slightly below the σ' values measured in sample P2. Comparing the LF Cole–Cole models in Fig. 10(d) (bold blue lines) with the inverted TD SIP data in the model cell at 3.4–4.5 m in Fig. 10(g) (bold blue line), it is clear that there is a good agreement at low frequencies between the inverted model cell Cole–Cole parameters and the FD IP spectra from samples P1 and P2. Note that the HF Cole–Cole models in Figs 10(d) and (e) (dashed lines) are only shown for information. They are not relevant to compare to the TD IP results since these were inverted with a single Cole–Cole model parametrization (eq. 1). No double Cole–Cole model parametrization for spectral inversion of TD IP data could be applied, because a wider acquisition range (bigger than 4 decades) would be necessary for resolving the eight parameters of a double Cole–Cole model. Therefore, the HF spectral information contained in the TD IP data was not extracted in this study.

The model cells at 5.9–7.4 m and 7.4–9.2 m depth in Fig. 10(b) (bold green lines) represents rectangle B discussed above. Sample P3 is located in the centre of the model cell at 5.9–7.4 m, whereas sample P4 is located in the very top of the deeper model cell at 9.2–11.2 m. In Fig. 10(b), a very good match can be observed between sample P3 and the model cell at 5.9–7.4 m, as well as between sample P4 and the model cell at 7.4–9.2 m. In both cases, the inverted σ_0 values are slightly lower compared to the σ' values from the laboratory data. In Fig. 10(h), the σ''_{max} peaks of the inverted model cells are located at around 2–3 Hz and the magnitude of σ''_{max} decrease with depth (between 5.9 and 11.2 m). The FD IP spectra of samples P3 and P4 are not Cole–Cole shaped, and the relaxation time has no meaning in materials with such frequency dispersion (therefore, the σ'' spectra were not fitted with double Cole–Cole models in Fig. 10e). However, the inverted σ''_{max} values (∼0.025–0.03 mS m^{-1}) are in agreement with the FD SIP data of P3 and P4 at low frequencies (∼0.01–0.1 Hz).

Rectangle C discussed above is represented by the model cells at 13.4–16.0 m, 16.0–19.0 m and 19.0–22.4 m in Fig. 10(c) (bold red lines). Sample P5 is located in the deeper part of the shallower of these model cells, while sample P6 is located across the border between both of the deeper ones. Fig. 10(c) shows that the σ_0 data is slightly higher in the inverted model cells compared to σ' from the laboratory data. In Fig. 10(i), the σ''_{max} peak is located at around 0.3–0.4 Hz in the inverted cell at 13.4–16.0 m, that is at higher frequencies compared to the relaxation time of the LF Cole–Cole model fitted to sample P5 in Fig. 10(f). In deeper model cells, the peak shifts towards lower frequencies in the inverted data (∼0.1 Hz), while the peak of sample P6 is located around 0.2–0.3 Hz (Fig. 10i). For sample P6, the maximum σ'' values are in the same range as the inverted model cell σ''_{max} values (∼0.01–0.02 mS m^{-1}), while the maximum σ'' values of sample P5 are lower (∼0.005 mS m^{-1}). Concerning the fact that the model cells are in between 2.6 and 3.4 m deep, the inverted Cole–Cole parameter still matches the laboratory data relatively well.

In summary, there is a generally good agreement between the inverted Cole–Cole parameters from the TD IP field data and the low-frequency part of the FD IP spectra measured in the laboratory. All parameter values in the model cells are in the same range as the respective core samples, and similar trends with depositional depth as in the FD IP spectra (see above) can be observed also in the field TD SIP data. The inverted field TD SIP data are, however, affected by horizontal and vertical constraints that makes a direct comparison complicated. It is, for example, likely that the model cell at depth 4.5–5.9 m in Figs 10(g) and (h) is affected by the relatively large shift in Cole–Cole parameters between its neighbouring model cells, and therefore match sample P3 (6.1–6.5 m) better than sample P2 (5.2–5.4 m). Similarly, the large increase in σ_0 values in the model cell at depth 19.0–22.4 m (Fig. 10c) is likely affected by the large increase in conductivity below the K–Pg boundary.

Interpretation of spectral TD IP tomography

In Fig. 11, 3-D views of all inverted parameter sections for both Line 1 and Line 2 are shown. The inverted models match well at the intersection, which increases the confidence of the inverted results and indicates that the inverted models are good representations of the electrical properties in the ground. The difference between the Palaeogene and the Cretaceous limestone can only be evaluated in the σ_0 model (Fig. 11a), as the K–Pg boundary is below the DOI of the Cole–Cole parameters in Figs 11(b)–(d). As already stated above, the σ_0 model captures the shift from Palaeogene to Cretaceous limestone well.

The inverted σ_0 values are relatively low in the uppermost few meters of the σ_0 model, likely due to the unsaturated zone between ∼0–2 m depth. Below this is a layer of slightly elevated σ_0 (encircled with a dashed line in Fig. 11a), before the σ_0 values decrease to very low values at elevations between ∼−50 and −60 mamsl. These elevations correspond to the zone with prominent flint bands and dense limestone identified in the borehole logging data (Fig. 3a). This is also the zone from where the low conductive samples P5 and P6 originate (Fig. 5a).

In the σ''_{max} model (Fig. 11b), an approximately 10-m-thick layer can be observed in the uppermost part of the section (∼−40 to −50 mamsl, marked with white dashed lines). The thickness and

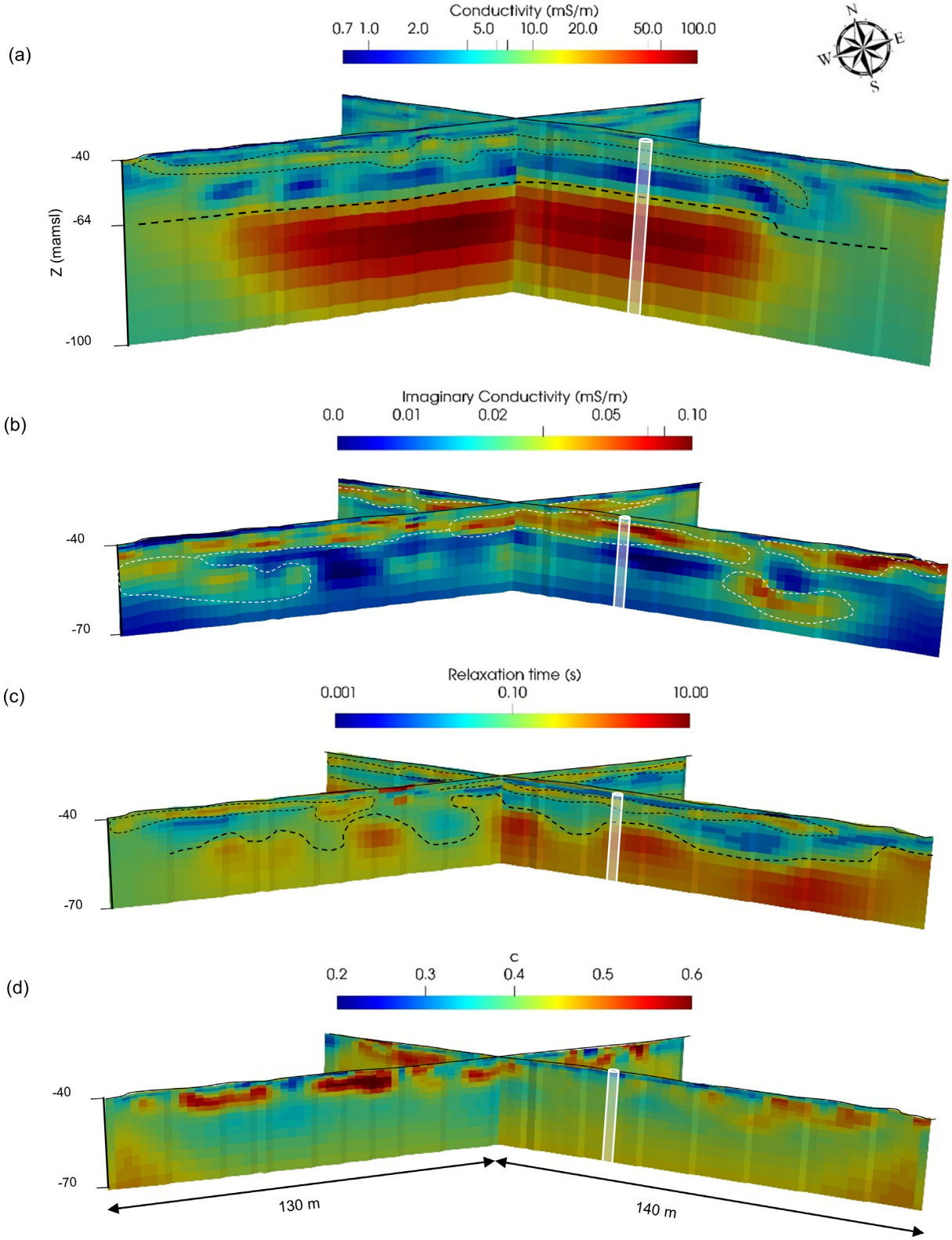

Figure 11. 3-D view showing the inverted results from Line 1 and Line 2 together with the location of the core. (a) Conductivity, (b) imaginary conductivity, (c) relaxation time and (d) frequency exponent.

elevation of this layer correspond to the expected location of the locally recognized middle Danian limestone unit (Brotzen 1959). It is possible that the microstructure of the middle Danian limestone, with the presence of coralline limestone and increased biodiversity, entails a stronger polarization of the material here compared to the lower Danian limestone (∼−50 to −60 mamsl).

In the τ_σ model (Fig. 11c), zones with high τ_σ are encircled with dashed lines. High τ_σ values are found in the lower part of

the model as well as in smaller zones and thin layers closer to the ground surface. The topography of the border between smaller and larger τ_σ at around −50 to −55 mamsl likely reflects the carbonate mound structures in the Danian limestone (e.g. Thomsen 1976). The elevation also corresponds well to the expected shift between lower to middle Danian deposits (see above; Brotzen 1959). The Danian mound structures in the eastern part of the Limhamn quarry have previously been investigated by Nielsen *et al.* (2004) with Ground Penetrating Radar (GPR) from the second 'floor', that is from the same elevation as the measurements in our study. The GPR data showed that typical mounds were 5–10 m high and occurred with 30–60 m spacing. Although the depth penetration of the GPR data were limited to around 10 m (Nielsen *et al.* 2004), the vertical and horizontal geometry of the carbonate mounds corresponds well to the topography of the deep τ_σ layer in our models (Fig. 11c). In Fig. 9, for example, it can be observed that the distance between the two τ_σ anomalies closest to the borehole is ∼40 m. Therefore, we interpret the shift between shorter and longer τ_σ values around −50 to −55 mamsl as the shift between the lower and middle Danian limestone. The longer relaxation times are interpreted as a reflection of bryozoan fragment dominance of the grains in the carbonate texture, as these fossils typically have elongated cylindrical shapes (e.g. Thomsen 1976) and the relaxation time generally is considered to be proportional to grain size (e.g. Leroy *et al.* 2008; Revil & Florsch 2010). A field photograph with stacks of bryozoan mounds visible at the quarry rock wall of the survey area (eastern border, see Fig. 1) is shown in Fig. 12.

The generally shorter inverted τ_σ values of the middle Danian limestone in Fig. 11(c) (above ∼ −50 mamsl) is interpreted as a possible consequence of the presence of coralline fossils and larger biodiversity, which likely entails more size (and shape) variation among the rock-forming carbonate components. Samples P3 and P4 originate from these elevations, and the FD SIP data from these cores showed spectral shapes where σ'' increased with frequency (Fig. 5c). This could reflect a broad range of grain sizes in the material and no clear dominant relaxation time representative of the samples. The comparison of the laboratory FD IP data with the inverted TD IP data in Fig. 10(b) showed that relatively high inverted τ_σ values were obtained at these levels, despite the fact that P3 and P4 were not Cole–Cole shaped.

As already discussed, the microstructures of the middle Danian limestone are expected to be less homogeneous than the lower Danian limestone. Studies of material from the same formation in Denmark showed that the middle Danian limestone can consist of three different types of facies; bryozoan limestone, coralline limestone and a transitional facies. Furthermore, the coralline limestones can be divided into several subfacies types (Bernecker & Weidlich 1990). In our data, smaller zones and thin layers of elevated τ_σ within the middle Danian limestone (Fig. 11c), such as the layer between samples P1 and P2, can possibly be interpreted as bryozoan-rich zones within the middle Danian deposits. Complex patterns can also be observed in parts of the $\sigma''_{\max}$ models in Fig. 11(b). Zones of high $\sigma''_{\max}$ values are not only found in the uppermost 10 m of the models but also at deeper levels in the southeastern and southwestern parts of the inverted sections. It is possible that enhanced polarization at deeper levels could also, together with the patterns in the τ_σ model discussed above, reflect bioherm structures within the limestone.

The c model in Fig. 11(d) is more challenging to interpret. The lowest c values can be observed in the most shallow model layers and can possibly be related to looser bedrock structure close to the ground surface (the uppermost part of the drill core was typically fractured and weathered). Anomalously high c values are only found in certain zones within the upper ∼10 m of the limestone. These zones can possibly be interpreted as non-cemented limestone (as indicated by samples P1 and P2 from the same levels in the core). However, this interpretation cannot be substantiated as no zones with very high inverted c values were covered by the core drilling.

DISCUSSION

Method and data uncertainties

All collection of data comes with a degree of uncertainty in the results. In this study, it was considered important to preserve the natural groundwater in the core samples for the FD SIP measurements. This resulted in relatively large core samples as fast measurements were prioritized over attempts to drill out smaller and more homogeneous samples from the core. The main uncertainties of the laboratory FD SIP data in this study are thus related to the sample geometry. Several of the relatively large core samples were more or less heterogeneous on a macroscopic scale. Such heterogeneities are, for example presence of flint nodules or gradually changing grain abundance/size distributions. However, the potential electrodes were placed in the central part of the cores where most of them appeared homogeneous on a macroscopic scale. Another uncertainty related to the sample geometry is that the sample cores in this study were of varying lengths. Although many sample cores were close to or exceed the ideal sample length (36.6 cm), some were shorter (minimum 17.5 cm). For the short samples, the potential electrodes were placed as far from the current electrodes as possible to avoid electrode polarization errors and increase the likelihood of homogeneous current distribution at the measurement points. Despite this, a theoretical risk of lower data quality of the shorter cores remains. However, the real- and imaginary conductivity results from samples C4 (30.2 cm long) and C5 (17.5 m long) are very similar despite the differences in sample length and electrode positions (see Figs 5d and f). C4 and C5 can be considered as replica samples, as both the optical macrostructures, carbonate textures and the measured physicochemical properties of these samples are essentially identical (see Table 1 and Fig. 4). The similar spectra from C4 and C5 therefore indicate that the quality of the FD SIP data is adequate for our purposes despite theoretical uncertainties related to varying sample lengths.

The results of the field spectral TD IP tomography, measured in 2-D, are subjected to all of the well-known uncertainties and assumptions involved with the method itself. These are, for example, deviation from a 2-D environment, difficulties in identifying noise in the data as well as processing and inversion uncertainties. The sedimentary rock at the field site in this study justifies the assumption of a 2-D environment, and no indications of, for example 3-D effects from the vertical walls around the quarry bottom of the field site were indicated in the inverted results. The diagonal placement of the measurement profiles as well as the separated cable layout and the low electrode contact resistances minimized the risk of both 3-D effects and capacitive coupling noise in the data sets (Dahlin & Leroux 2012). Moreover, the location of the field site itself which is nature protected and distant to urban infrastructure also limits the risk of electrical noise and 3-D effects. Remaining systematic noise and instrument drift were successfully handled with the automatic processing scheme presented by Olsson *et al.* (2016).

The main uncertainties in the inverted TD SIP results are related to the manual processing and inversion. In this study, an attempt of

Figure 12. Field photograph showing quarry rock wall (∼13 m high) with stacks of bryozoan mounds visible (outlines indicated by stippled lines), view approximately towards W–NW. The TD IP tomography survey and core drilling was performed on the 'plateau' above.

performing a systematic manual processing of the IP decays was made. Inductive coupling effects are always present in IP decays and varies with both geometric factor and the magnitude of the signals (Fiandaca 2018). These effects are often clearly visible in the decays as a significant change of slope. The theoretical results presented by Fiandaca (2018) justifies the removal of early time windows in this study. However, for some decays, difficulties in distinguishing inductive effects in the data remain, especially for decays with large geometric factors and small signal levels. For unknown reasons, Line 1 was generally more noisy and contained more corrupted decays compared to Line 2, and more data were therefore removed from Line 1. Since more than 90 per cent of the decays were kept in both data sets, the inverted results are unlikely to be significantly biased by the manual processing.

The processed data were successfully inverted for spectral parameters and the use of long pulse times (8 s) improved the resolution of the spectral parameters (Fiandaca *et al.* 2018). The χ values of the inversion results show that the inverted models fit the data well except at the earliest time gates, and the match where the inverted profiles cross each other gives further confidence in the inverted models. The higher early-time misfit is probably due to high-frequency spectral content present in the data, but not modeled in this study because the inversion process becomes too much ill-posed when using a double Cole–Cole parametrization, necessary for fitting the laboratory spectra.

In addition to technical data quality uncertainties, the comparison between laboratory and field measurements also implies uncertainties related to the differences in ambient environmental conditions. Firstly, there is a slight risk that the groundwater conditions preserved in the cores are not identical to the field conditions. Although the core pieces were vacuum-sealed in plastic bags immediately after the core recovery, small defects in the plastic seal could lead to evaporation and water contents that do not represent completely water-saturated conditions. Defects in the plastic seal could also lead to different redox conditions in the preserved cores and thus an altered groundwater composition. Secondly, the laboratory measurements were performed at ambient room temperature (23 ± 2 °C) while the natural groundwater temperatures were significantly lower during the field measurements (∼6–10 °C at 2–25 m below the ground surface). Binley *et al.* (2010) investigated the temperature dependence of three sandstones in a range between 5 and 30 °C and measured an increase in both σ' and σ'' of ∼2 per cent $(°C)^{-1}$. Similar results were observed by Bairlein *et al.* (2016), who investigated 13 different sandstone samples in an extended temperature range (0–40 °C). In both studies, the position of the σ'' peak shifted towards higher frequencies with increasing temperatures (Binley *et al.* 2010; Bairlein *et al.* 2016).

Comparison between field TD IP and laboratory FD IP

Despite the data uncertainties discussed above and the differences between the field and laboratory methods, the inverted Cole–Cole parameters from the field TD IP data were generally in good agreement with the low-frequency part of the laboratory FD IP data. The comparison in this study is only relevant for low frequencies, as the MIC model used for the inversion only fits a single Cole–Cole relaxation and does not consider the increase in imaginary conductivity that is usually present at higher frequencies (see Figs 5c and f).

The frequency range of the FD IP data measured in this study is 0.01–20 000 Hz (although inductive coupling effects are likely in data above ∼1000 Hz and therefore not used for interpretation). With the type of TD waveform used for the field measurements here, the theoretical spectral range (limited by the waveform period and sampling frequency) corresponds to 0.0625–1875 Hz in FD. However, the actual spectral range is decreased by the gating of the IP decays and the removal of early time gates during the processing. For more than 50 per cent of the processed IP decays in Line 2, the first time gate has the centre time 2.85 ms (Fig. 2). According to Fiandaca (2018), this means that frequencies above ∼351 Hz are not present in the processed TD data. However, as mentioned above, the data at high frequencies/short times are not relevant to compare in this study. More important is that the spectral ranges of the TD and FD measurements are comparable at the low-frequency end, which is also often the only part of the FD IP spectra that is interpreted.

Research focusing on measurement scale effects on Cole–Cole parameters is rare, but Maineult *et al.* (2017) studied upscaling effects of Cole–Cole parameters from pore scale to sample scale with a simplified random tube network modelling approach. Their results showed that similar bulk Cole–Cole parameters were obtained for both homogeneous and heterogeneous 2-D distributions of different pore sizes, thus indicating that 2-D heterogeneity might not affect measured bulk Cole–Cole parameters as long as the pore size distribution is the same within the modelled area. The comparison of

inversion model cells with core samples in this study is, however, a more complex problem. In addition to heterogeneity differences, another expected effect of the scale differences was that variations in microstructural patterns would be larger within the model cells compared to the core samples. Since these patterns govern the SIP data, large variations within the blocks can be expected to result in more dispersed spectra without clear relaxation peaks. Furthermore, the inverted data is, in contrast to the FD IP spectra, affected by inversion constraints and a resolution that decrease with depth. Considering all these differences, the problem with scale effects can be considered to be relatively low for our data. In Figs 10(d) and (g), the LF Cole–Cole model shapes are similar for the FD IP spectra (P1 and P2) and the inverted TD IP data (bold blue lines). At deeper levels (Figs 10f and i), the order of magnitude of the values and approximate spectral shapes are similar (P5 and P6). Exceptions are samples P3 and P4, where the FD SIP data indicate spectral shapes increasing with frequency and the inversion software tends to fit Cole–Cole models with relatively narrow width (low c values, Figs 10e and h). The reason for this disparity cannot be explained by our data. It is theoretically possible that the inverted data represents real material properties, since larger volumes than the corresponding core samples are sensed. However, since the σ'' values at the lowest frequencies of the FD IP data corresponds well to the values at 1 Hz in the TD data, it is more likely that τ_σ and c are more constraint-driven in the inversion model cells at these elevations due to an absence of a clear relaxation in the data. Either way, the Cole–Cole model cannot take any shape that represent the spectral shapes of P3 and P4, that is σ'' increasing with frequency.

Another difference that was expected to affect the comparison of the spectral FD IP and TD IP data was the ambient temperature difference between field and laboratory conditions. Fig. 9(a) shows that the σ' values measured at samples P3 and P4 were ∼10–15 per cent higher (at 1 Hz) than the inverted σ_0 values at the corresponding levels. This difference could possibly be temperature related, although a larger increase would be expected according to previous experimental results (Binley *et al.* 2010, Bairlein *et al.* 2016). For the data measured at the levels of samples P5 and P6, the opposite pattern can be observed. Here, the inverted σ_0 values are slightly higher than the σ' values measured in laboratory. A likely explanation is that the laboratory data is measured on cores where the bedding is perpendicular to the current path. Presence of flint bands and dense layers in the limestone at this depth (see Fig. 3a) are likely to obstruct the current path and decrease the measured σ' of the samples. During the field measurements on the other hand, the current path can be expected to be nearly parallel to the bedding (assuming the current distribution of a homogeneous half-space), or at least have a larger degree of freedom to take available paths of least resistance.

Another interesting case of anisotropy is sample C3, where the clay bedding is clearly perpendicular to the current path (Figs 4j and s). The notably high σ'' values measured at this sample might be explained not only by the high clay content but also by the direction of the measurement. While sand-clay mixtures are known to produce elevated σ'' values due to the high surface area and cation exchange capacity of clay minerals (e.g. Vinegar & Waxman 1984; Slater & Lesmes 2002b), the layered geometry of pure clays might short-circuit the polarization mechanism (Marshall & Madden 1959). Therefore, measurements perpendicular to the bedding likely result in high σ'' values as observed for sample C3 (Fig. 5f). Systematic experimental studies of anisotropy effects on SIP measurements are rare, but an example of strong effects of anisotropy in a sandstone sample has been reported by Zisser *et al.* (2010a) while anisotropic shales were measured with SIP in Woodruff *et al.* (2014).

Varying spectral IP responses of limestone

One of the main aims of this study was to investigate the spectral response of limestone and analyse possible sources of observed variations. Previous studies of SIP responses in limestones are rare. In a study focusing on other materials, Ghorbani *et al.* (2009) used porous limestone samples saturated with conductive brine in order to test the SIP experimental setup on non-polarizable materials. Kremer *et al.* (2016) observed σ'' values increasing from ∼0.001 to 0.01 mS m^{-1} between 0.1 and 1000 Hz in a carbonate sand sample. According to Zhang *et al.* (2012), the surface charge is relatively low on calcium carbonate minerals compared to silica minerals, which might explain why low or absent polarization is sometimes observed. However, the composition and structure of limestones vary significantly. In a previous TD IP tomography survey, the inverted Cole–Cole results indicated large variations within a limestone formation (Johansson *et al.* 2016).

A few publications dealing with systematic studies of SIP variations in limestone samples exist. Halisch *et al.* (2014) presented results from SIP measurements on Egyptian late Cretaceous limestone samples, described as molluscan chalkey limestones, with glauconitic content of 3.4–26 per cent and varying carbonate textures (packstone, grainstone and floatstone). Four different typical spectral shapes of φ data were presented, which occurred randomly among the different groups of carbonate textures. No correlation between the specific surface area to porosity ratio (S_{por}) and σ'' was found, despite the well-proven relationship between these parameters in sandstones (Weller *et al.* 2015). More recently, Hupfer *et al.* (2017) reported results from SIP measurements on four groups of carbonates including limestones and dolomites. The σ' values were less than 11 mS m^{-1} for all samples and the shape of the σ'' spectra varied for each group (Hupfer *et al.* 2017). However, no clear relationships between properties of the samples and the SIP responses were shown in this study.

In the present study, the FD IP spectra measured on different limestone samples resulted in a large variation of spectral shapes and polarization magnitudes. The main differences were found between the Cretaceous and the Palaeogene sample groups, which represent two distinct types of limestone in terms of general characteristics. High σ' values (∼200–600 mS m^{-1}) were measured on all Cretaceous samples, and the σ'' values increased with frequency from 0 to ∼2 mS m^{-1} (C4 and C5) or ∼0.5 mS m^{-1} (C1, C2 and C6) at 10 Hz. The only exception was the clay-laminated sample C3 with higher content of siliciclastic minerals and iron-rich minerals discussed above. In terms of carbonate texture, all Cretaceous samples were classified as carbonate mudstone with some presence of siliciclastic clay minerals according to the XRF results.

The σ' and σ'' data of the Palaeogene samples in this study are in the same order of magnitude as the data presented by Hupfer *et al.* (2017), with σ' values below 9 mS m^{-1} and σ'' values below 0.2 mS m^{-1} at frequencies from 0.01 to 10 Hz. In agreement with Halisch *et al.* (2014), no obvious relationships between the φ spectra and carbonate texture were found in our study. However, the σ'' data seem to be related to lithological properties. Cole–Cole shaped spectra were measured on the four Palaeogene samples with the highest dry density (2.36–2.47 g/cm^3) and lowest water contents (0.8–4.1 per cent). The Palaeogene samples with spectral shapes

of increasing σ'' values (P3, P4 and P7) all had densities below 2.15 g/cm^3 and porosities larger than 6.1 per cent.

The Cole–Cole relaxation time is generally considered to be directly related to the dominant pore-throat size in sandstones (e.g. Scott & Barker 2003; Binley *et al.* 2005; Zisser *et al.* 2010a) which in turn is correlated with the dominant grain size (Titov *et al.* 2002; Revil *et al.* 2012). All Palaeogene samples in this study consist of a relatively high proportions of coarse (sand-sized or larger) carbonate grains in relation to matrix (silt- or finer-sized carbonate particles). The proportion of grains in the carbonate texture can be viewed as a substitute for dominant or average grain size in the samples as explained above. The similar proportion of grains in samples P1 and P2 can thus be interpreted as similar grain size distributions in these samples (∼26 per cent grains) while the carbonate texture is coarser and the dominant or average grain size is thus likely larger in P5 (∼58 per cent grains). In the FD SIP data, this difference in carbonate texture and thus assumed dominant grain size is reflected by the large τ values of P5 compared to P1 and P2. P6 deviates from this pattern; despite having slightly coarser carbonate texture (30 per cent grains) than P1 and P2, the measured τ value is smaller for P6. This could possibly be an effect of extremely low porosity (0.8 per cent compared to 2.3–4.1 per cent for P1, P2 and P5). Scott & Barker (2003) showed that the pore throat size distribution is affected by the compaction of grains. Denser packing of grains (of the same size) tends to give rise to a dominance of smaller pore throat sizes in the samples and, thus, shorter measured relaxation times (Scott & Barker 2003). Similar trends were also found by Binley *et al.* (2005) and Zisser *et al.* (2010a).

Our results also suggest a possible relationship between σ'' at low frequencies and presence of calcite cement in the limestone samples. Below 1 Hz, the σ'' values are largest for the cement-free samples (P1 and P2). The values are intermediate in the samples with 1–2 per cent cement (P3, P4 and P7) and very low for the sample with 12 per cent cement (P5). An exception to this trend is sample P6 with 1 per cent cement and low σ'' values. Previous research shows that the effect of calcite on the IP of a granular material is dependent on the background polarizability as well as the morphology of the calcite. Calcite precipitation experiments in silica gel columns suggest a decrease of measured σ'' after calcite precipitation taking place at grain-grain contacts in the material (Zhang *et al.* 2012). Comparable results were also found by Wu *et al.* (2010) after the formation of calcite aggregates extending across several grains in their experimental columns. Wu *et al.* (2010) interpreted the effect as a result of reduced surface area due to the aggregate calcite structure in a polarizable media. In contrast, precipitation of isolated small calcite crystals in the pore structure of the material instead tended to increase the surface area, σ'' as well as the relaxation time (Wu *et al.* 2010).

Because of the limited data set and large variation of sample properties in this study, all SIP variations cannot be explained conclusively. The results are likely affected by a combination of chemical composition, physical bulk parameters, carbonate texture and carbonate grain shapes. In another study, smaller core samples and more systematic variations of one or two properties could probably yield more knowledge about the mechanisms behind observed variations of SIP responses in limestones.

CONCLUSIONS

In this study, we found a good agreement between inverted Cole–Cole parameters from TD IP tomography and the low frequency part of FD IP spectra measured on core samples in a laboratory environment. Despite large differences in scale, measurement methods and environmental conditions, all measured values were in the same range for all parameters. Some deviations between the TD and FD methods were observed, but the uncertainties these deviations bring can be considered small compared to the caution that should always be taken when inverted field data are interpreted. We therefore conclude that it is possible to retrieve Cole–Cole parameters from spectral TD IP field tomography that are comparable to values obtained for samples with FD SIP systems. This opens up large possibilities for the interpretation of inverted field data, as the comprehensive knowledge about the relationships between lithological properties and Cole–Cole parameters from laboratory studies can be directly related to field data.

We also conclude that limestones can give rise to a wide range of spectral responses. Carbonate texture seems to have an important control over the electrical properties of the material, as the largest differences were found between the fine-grained matrix-dominated Cretaceous limestone and the coarser Palaeogene limestones with more abundant sand-sized grains and common presence of crystalline cement. In the Palaeogene limestone, Cole–Cole shaped spectra were observed in four out of seven samples and the relaxation time is likely related to the dominant size (and/or shape) of the carbonate fossil grains. These results are analogous to variations of spectral responses in sandstones, but differences can also be expected as, for example, grain shapes and sizes can vary considerably in limestone materials.

The results from the spectral TD IP tomography showed that the method efficiently can discriminate between different lithologies. The K–Pg boundary was clearly visible in the conductivity data, while the Cole–Cole parameters indicated lithological differences within the Palaeogene limestone, including large-scale bryozoan dominated bioherm structures.

ACKNOWLEDGEMENTS

The authors would like to thank Mats Wirén and Malmö kommun for allowing this research project access to the Limhamn quarry. The core drilling and parts of the analyses were funded by the Royal Physiographic Society in Lund. We acknowledge Riksriggen for provision of facilities and experimental support and we would like to thank Jan-Erik Rosberg, Johan Kullenberg and Simon Rejkjær from Lund University for assistance. Riksriggen receives funding through the Swedish Research Council under the grant no 2017-00642. We would also like to thank Per-Gunnar Alm and Matteo Rossi for carrying out the borehole logging and Per-Ivar Olsson, Matteo Rossi and Tina Martin from Lund University as well as Richard Mutafela from Linnaeus University in Kalmar for field assistance during the DCIP measurements. Funding which made this work possible was provided by BeFo, Swedish Rock Engineering Research Foundation, (ref. 331) and SBUF, The Development Fund of the Swedish Construction Industry, (ref. 12719 and 13232) and Formas, The Swedish Research Council for Environment, Agricultural Sciences and Spatial Planning, provided funding for this presentation of the results (ref. 2012-1931) as part of the Geoinfra-TRUST framework (http://www.trust-geoinfra.se/). Sara Johansson wrote the paper and Anders Lindskog and Torleif Dahlin contributed with suggestions and critical reviews of the text. Sara Johansson and Anders Lindskog planned the field work and performed it together with others. Sara Johansson and Anders Lindskog carried out the laboratory work. Sara Johansson and Gianluca Fiandaca processed

and inverted the field data. Sara Johansson analysed and interpreted the geophysical data and Anders Lindskog analysed the geological data.

REFERENCES

Auken, E. *et al.*, 2014. An overview of a highly versatile forward and stable inverse algorithm for airborne, ground-based and borehole electromagnetic and electric data, *Explor. Geophys.,* **46**(3), 223–235.

Auken, E., Viezzoli, A. & Christiansen, A.V., 2009. A single software for processing, inverting, and presentation of AEM data of different system: the Aarhus Workbench, in *Proceedings of the Australian Society of Exploration Geophysicist (ASEG), 2009*, Sydney, Australia, pp. 1–5.

Bairlein, K., Bücker, M., Hördt, A. & Hinze, B., 2016. Temperature dependence of spectral induced polarization data: experimental results and membrane polarization theory, *Geophys. J. Int.,* **205**(1), 440–453.

Bergström, J., Holland, B., Larsson, K., Norling, E. & Sivhed, U., 1982. *Guide to Excursions in Scania. Sveriges Geol. Undersökning Ca 54,* Ca 54., Sveriges Geologiska Undersökning.

Bernecker, M. & Weidlich, O., 1990. The Danian (Paleocene) coral limestone of Fakse, Denmark: a model for Ancient Aphotic, Azooxanthellate Coral Mounds, *Facies,* **22,** 103–137.

Binley, A., Kruschwitz, S., Lesmes, D. & Kettridge, N., 2010. Exploiting the temperature effects on low frequency electrical spectra of sandstone: a comparison of effective diffusion path lengths, *Geophysics,* **75**(6), A43–A46.

Binley, A., Slater, L.D., Fukes, M. & Cassiani, G., 2005. Relationship between spectral induced polarization and hydraulic properties of saturated and unsaturated sandstone, *Water Resour. Res.,* **41**(12), W12417.

Brotzen, F., 1959. *On Tylocidaris species (Echinoidea) and the stratigraphy of the Danian of Sweden with a bibliography of the Danian and the Paleocene: with a bibliography of the Danian and the Paleocene,* Sveriges Geologiska Undersökning.

Brusatte, S.L. *et al.*, 2015. The extinction of the dinosaurs, *Biol. Rev.,* **90**(2), 628–642.

Dahlin, T., 2014. Factors affecting time domain IP data quality, in *Proceedings of the 3rd International Workshop on Induced Polarization,* 6–9 April 2014, Ile d'Oléron, France, pp. 50–51.

Dahlin, T. & Leroux, V., 2012. Improvement in time-domain induced polarization data quality with multi-electrode systems by separating current and potential cables, *Near Surf. Geophys.,* **10,** 545–565.

Dahlin, T. & Zhou, B., 2006. Multiple-gradient array measurements for multichannel 2D resistivity imaging, *Near Surf. Geophys.,* **4**(2), 113–123.

Doetsch, J., Ingeman-Nielsen, T., Christiansen, A. V., Fiandaca, G., Auken, E. & Elberling, B., 2015. Direct current (DC) resistivity and induced polarization (IP) monitoring of active layer dynamics at high temporal resolution, *Cold Reg. Sci. Technol.,* **119,** 16–28.

Dunham, R.J., 1962. Classification of carbonate rocks according to texture, *Classif. Carbonate rocks,* **1,** 108–121.

Fiandaca, G., 2018. Induction-free acquisition range in spectral time- and frequency-domain induced polarization at field scale, *Geophys. J. Int.,* doi: 10.1093/gji/ggy409.

Fiandaca, G., Auken, E., Christiansen, A.V. & Gazoty, A., 2012. Time-domain-induced polarization: full-decay forward modeling and 1D laterally constrained inversion of Cole-Cole parameters, *Geophysics,* **77**(3), E213–E225.

Fiandaca, G., Christiansen, A. V. & Auken, E., 2015. Depth of investigation for multi-parameters inversions, in *Proceedings of Near Surface Geoscience 2015 - 21st European Meeting of Environmental and Engineering Geophysics*, Torino, Italy, pp. 6–10.

Fiandaca, G., Madsen, L.M. & Maurya, P.K., 2018. Re-parameterizations of the Cole-Cole model for improved spectral inversion of induced polarization data, *Near Surf. Geophys.,* **16**(4), 385–399, .

Fiandaca, G., Ramm, J., Binley, A., Gazoty, A., Christiansen, A. V. & Auken, E., 2013. Resolving spectral information from time domain induced polarization data through 2-D inversion, *Geophys. J. Int.,* **192**(2), 631–646.

Flügel, E., 2010. *Microfacies of Carbonate Rocks: Analysis, Interpretation And Application,* Springer Verlag.

Ghorbani, A., Cosenza, P., Revil, A., Zamora, M., Schmutz, M., Florsch, N. & Jougnot, D., 2009. Non-invasive monitoring of water content and textural changes in clay-rocks using spectral induced polarization: a laboratory investigation, *Appl. Clay Sci.,* **43**(3–4), 493–502.

Halisch, M., Weller, A., Hupfer, S. & Kassab, M., 2014. Impedance spectroscopy on carbonates, in *Proceedings of the International Symposium of the Society of Core Analysts* , 8–11 September 2014, Avignon, France, pp. 1–6.

Hupfer, S., Halisch, M. & Weller, A., 2017. Using low frequency electrical impedance spectroscopy for an enhanced pore space characterization and assessment of carbonates, in *Proceedings of the International Symposium of the Society of Core Analysts,* 27–30 August 2017, Vienna, Austria, pp. 1–8.

Ingeman-Nielsen, T., Tomaškoviová, S. & Dahlin, T., 2016. Effect of electrode shape on grounding resistances—Part 1: the focus-one protocol, *Geophysics,* **81**(1), WA159–WA167.

Johansson, S., Rossi, M., Hall, S.A., Sparrenbom, C., Hagerberg, D., Tudisco, E., Rosqvist, H. & Dahlin, T., 2019. Combining spectral induced polarization with x-ray tomography to investigate the importance of DNAPL geometry in sand sample, *Geophysics,* **84**(3), 1–93.

Johansson, S., Sparrenbom, C., Fiandaca, G., Lindskog, A., Olsson, P.-I., Dahlin, T. & Rosqvist, H., 2016. Investigations of a Cretaceous limestone with spectral induced polarization and scanning electron microscopy, *Geophys. J. Int.,* **208**(2), 954–972.

Johnson, I.M., 1984. Spectral induced polarization parameters as determined through time-domain measurements, *Geophysics,* **49**(11), 1993–2003.

Kemna, A., 2000. *Tomographic Inversion of Complex Resistivity - Theory and Application,* Ruhr-Universität Bochum.

Kremer, T., Schmutz, M., Maineult, A. & Agrinier, P., 2016. Laboratory monitoring of CO_2 injection in saturated silica and carbonate sands using spectral induced polarization, *Geophys. J. Int.,* **207**(2), 1258–1272.

Kruschwitz, S., Binley, A., Lesmes, D. & Elshenawy, A., 2010. Textural controls on low-frequency electrical spectra of porous media, *Geophysics,* **75**(4), WA113–WA123.

Leroy, P., Revil, A., Kemna, A., Cosenza, P. & Ghorbani, A., 2008. Complex conductivity of water-saturated packs of glass beads, *J. Colloid Interface Sci.,* **321**(1), 103–117.

Länsstyrelsen i Skåne län, 2016. *Bevarandeplan för Natura 2000-område Limhamns kalkbrott,* pp. 22, Länsstyrelsen Skåne.

Mackey, E.A., Lindstrom, R.M. & Murphy, K.E., 2010. *Certification of Three NIST Renewal Soil Standard Reference Materials for Element Content : SRM 2709a San Joaquin Soil , SRM 2710a Montana Soil I , and SRM 2711a Montana Soil II NIST Special Publication 260-172 Certification of Three NIST Renewal Soil Sta*.

Madsen, L.M., Fiandaca, G., Auken, E. & Christiansen, A.V., 2017. Time-domain induced polarization - an analysis of Cole-Cole parameter resolution and correlation using Markov ChainMonte Carlo inversion, *Geophys. J. Int.,* **211**(3), 1341–1353.

Maineult, A., Revil, A., Camerlynck, C., Florsch, N. & Titov, K., 2017. Upscaling of spectral induced polarization response using random tube networks, *Geophys. J. Int.,* **209**(2), 948–960.

Major, J. & Silic, J., 1981. Restrictions on the use of Cole-Cole dispersion models in complex resistivity interpretation, *Geophysics,* **46**(6), 916–931.

Marshall, D.J. & Madden, T.R., 1959. Induced polarization, a study of its causes, *Geophysics,* **XXIV**(4), 790–816.

Maurya, P.K., Balbarini, N., Møller, I., Rønde, V., Christiansen, A. V., Bjerg, P.L., Auken, E. & Fiandaca, G., 2018a. Subsurface imaging of water electrical conductivity, hydraulic permeability and lithology at contaminated sites by induced polarization, *Geophys. J. Int.,* **213**(2), 770–785.

Maurya, P.K., Fiandaca, G., Christiansen, A.V. & Auken, E., 2018b. Field-scale comparison of frequency- and time-domain spectral induced polarization, *Geophys. J. Int.,* **214**(2), 1441–1465.

Nielsen, L., Boldreel, L.O. & Surlyk, F., 2004. Ground-penetrating radar imaging of carbonate mound structures and implications for interpretation of marine seismic data, *Am. Assoc. Petrol. Geol. Bull.,* **88**(8), 1069–1082.

Norbisrath, J. H., Eberli, G. P., Shen, S. & Weger, R. J., 2018. Complex resistivity spectra for estimating permeability in dolomites from the Mississippian Madison Formation, Wyoming, *Mar. Pet. Geol.,* **89,** 479–487.

Nordsiek, S. & Weller, A., 2008. A new approach to fitting induced-polarization spectra, *Geophysics,* **73**(6), F235–F245.

Olsson, P.-I., Dahlin, T., Fiandaca, G. & Auken, E., 2015. Measuring time-domain spectral induced polarization in the on-time: decreasing acquisition time and increasing signal-to-noise ratio, *J. appl. Geophys.,* **123,** 316–321.

Olsson, P.-I., Fiandaca, G., Larsen, J.J., Dahlin, T. & Auken, E., 2016. Doubling the spectrum of time-domain induced polarization by harmonic de-noising, drift correction, spike removal, tapered gating and data uncertainty estimation, *Geophys. J. Int.,* **207**(2), 774–784.

Pelton, W.H., Ward, S.H., Hallof, P.G., Sill, W.R. & Nelson, P.H., 1978. Mineral discrimination and removal of inductive coupling with multifrequency IP, *Geophysics,* **43**(3), 588–609.

Revil, A. & Florsch, N., 2010. Determination of permeability from spectral induced polarization in granular media, *Geophys. J. Int.,* **181,** 1480–1498.

Revil, A., Koch, K. & Holliger, K., 2012. Is it the grain size or the characteristic pore size that controls the induced polarization relaxation time of clean sands and sandstones?, *Water Resour. Res.,* **48**(5), W05602.

Scott, J.B.T. & Barker, R.D., 2003. Determining pore-throat size in Permo-Triassic sandstones from low-frequency electrical spectroscopy, *Geophys. Res. Lett.,* **30**(9), 1450.

Seigel, H.O., 1959. Mathematical formulation and type curves for induced polarization, *Geophysics,* **XXIV**(3), 547–565.

Shuey, R.T. & Johnson, M., 1973. On the phenomenology of electrical relaxation in rocks, *Geophysics,* **38**(1), 37–48.

Sivhed, U., Wikman, H. & Erlström, M., 1999. *Beskrivning till berggrundskartorna 1C Trelleborg NV and NO samt 2C Malmö SV, SO, NV and NO,* Sveriges Geologiska Undersökning.

Slater, L. & Lesmes, D.P., 2002a. Electrical-hydraulic relationships observed for unconsolidated sediments, *Water Resour. Res.,* **38**(10), 1213.

Slater, L.D. & Lesmes, D., 2002b. IP interpretation in environmental investigations, *Geophysics,* **67**(1), 77–88.

Tarasov, A. & Titov, K., 2013. On the use of the Cole-Cole equations in spectral induced polarization, *Geophys. J. Int.,* **195**(1), 352–356.

Thomsen, E., 1976. Depositional environment and development of Danian bryozoan biomicrite mounds (Karlby Klint, Denmark), *Sedimentology,* **23**(4), 485–509.

Titov, K., Komarov, V., Tarasov, V. & Levitski, A., 2002. Theoretical and experimental study of time domain-induced polarization in water-saturated sands, *J. appl. Geophys.,* **50**(4), 417–433.

Vanhala, H., 1992. Spectral IP studies of Finnish ore prospects, *Geophysics,* **57**(12), 1545–1555.

Vinegar, H.J. & Waxman, M.H., 1984. Induced polarization of shaly sands, *Geophysics,* **49**(8), 1267–1287.

Weller, A., Slater, L., Huisman, J.A., Esser, O. & Haegel, F., 2015. On the specific polarizability of sands and sand-clay mixtures, *Geophysics,* **80**(3), A57–A61.

Woodruff, W. F., Revil, A. & Torres-Verdín, C., 2014. Laboratory determination of the complex conductivity tensor of unconventional anisotropic shales, *Geophysics,* **79**(5), E183–E200.

Wu, Y., Hubbard, S., Williams, K.H. & Ajo-Franklin, J., 2010. On the complex conductivity signatures of calcite precipitation, *J. geophys. Res.,* **115,** G00G04.

Zarif, F., Kessouri, P. & Slater, L., 2017. Recommendations for field-scale Induced Polarization (IP) data acquisition and interpretation, *J. Environ. Eng. Geophys.,* **22**(4), 395–410.

Zhang, C., Slater, L., Redden, G., Fujita, Y., Johnson, T. & Fox, D., 2012. Spectral induced polarization signatures of hydroxide adsorption and mineral precipitation in porous media, *Environ. Sci. Technol.,* **46**(8), 4357–4364.

Zimmermann, E., Kemna, A., Berwix, J., Glaas, W., Münch, H.M. & Huisman, J.A., 2008. A high-accuracy impedance spectrometer for measuring sediments with low polarizability, *Meas. Sci. Technol.,* **19**(10), 1–9.

Zisser, N., Kemna, A. & Nover, G., 2010a. Relationship between low-frequency electrical properties and hydraulic permeability of low-permeability sandstones, *Geophysics,* **75**(3), E131–E141.

Zisser, N., Kemna, A. & Nover, G., 2010b. Dependence of spectral-induced polarization response of sandstone on temperature and its relevance to permeability estimation, *J. geophys. Res.,* **115**(9), 1–15.

Zonge, K.L., Sauck, W.A. & Sumner, J.S., 1972. Comparison of time, frequency and phase measurements in induced polarization, *Geophys. Prospect.,* **20**(3), 626–648.

SUPPORTING INFORMATION

Supplementary data are available at *GJI* online.

Please note: Oxford University Press is not responsible for the content or functionality of any supporting materials supplied by the authors. Any queries (other than missing material) should be directed to the corresponding author for the paper.